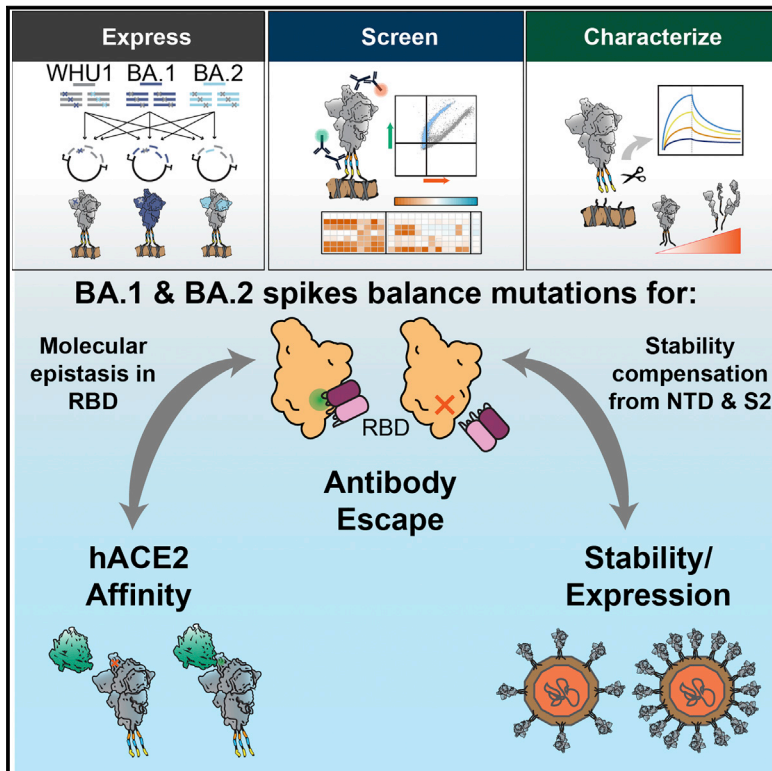


Cell Host & Microbe

Antibody escape and cryptic cross-domain stabilization in the SARS-CoV-2 Omicron spike protein

Graphical abstract



Authors

Kamyab Javanmardi,
Thomas H. Segall-Shapiro,
Chia-Wei Chou, ..., Andrew D. Ellington,
Ilya J. Finkelstein, Jimmy D. Gollihar

Correspondence

kjavanmardi@utexas.edu (K.J.),
ilya@finkelsteinlab.org (I.J.F.),
jgollihar2@houstonmethodist.org (J.D.G.)

In brief

The Omicron BA.1 and BA.2 variants have unprecedented numbers of nonsynonymous and indel spike protein mutations. Javanmardi et al. report the antigenicity, expression, and hACE2 affinity changes due to these mutations, in different protein contexts. This study reveals cryptic cross-domain interactions that enhance antibody escape and stabilize the spike protein.

Highlights

- The Omicron BA.1 and BA.2 spike proteins are antigenically distinct
- BA.1 and BA.2 RBDs balance antibody escape and human ACE2 binding
- Cryptic cross-domain interactions in Omicron spikes contribute to antibody escape
- Omicron NTD and S2 domains provide stability compensation to immune evasive RBDs

Short article

Antibody escape and cryptic cross-domain stabilization in the SARS-CoV-2 Omicron spike protein

Kamyab Javanmardi,^{1,*} Thomas H. Segall-Shapiro,² Chia-Wei Chou,¹ Daniel R. Boutz,^{1,2} Randall J. Olsen,^{2,3,4} Xuping Xie,⁵ Hongjie Xia,⁵ Pei-Yong Shi,⁵ Charlie D. Johnson,⁶ Ankur Annapareddy,¹ Scott Weaver,⁷ James M. Musser,^{3,4} Andrew D. Ellington,^{1,8} Ilya J. Finkelstein,^{1,8,*} and Jimmy D. Gollihar^{1,2,9,*}

¹Department of Molecular Biosciences, The University of Texas at Austin, Austin, TX, USA

²Laboratory of Antibody Discovery and Accelerated Protein Therapeutics, Center for Infectious Diseases, Houston Methodist Research Institute and Department of Pathology and Genomic Medicine, Houston Methodist Hospital, Houston, TX, USA

³Laboratory of Molecular and Translational Human Infectious Diseases Research, Center for Infectious Diseases, HMRI and Department of Pathology and Genomic Medicine, HMH, Houston, TX, USA

⁴Department of Pathology and Laboratory Medicine, Weill Cornell Medical College, New York, NY, USA

⁵Department of Biochemistry and Molecular Biology, University of Texas Medical Branch, Galveston, TX, USA

⁶Department of Biomedical Engineering, The University of Texas at Austin, Austin, TX, USA

⁷University of Texas Medical Branch, World Reference Center for Emerging Viruses and Arboviruses, Galveston, TX, USA

⁸Center for Systems and Synthetic Biology, The University of Texas at Austin, Austin, TX, USA

⁹Lead contact

*Correspondence: kjavanmardi@utexas.edu (K.J.), ilya@finkelsteinlab.org (I.J.F.), jgollihar2@houstonmethodist.org (J.D.G.)

<https://doi.org/10.1016/j.chom.2022.07.016>

SUMMARY

The worldwide spread of severe acute respiratory syndrome coronavirus 2 (SARS-CoV-2) has led to the repeated emergence of variants of concern. For the Omicron variant, sub-lineages BA.1 and BA.2, respectively, contain 33 and 29 nonsynonymous and indel spike protein mutations. These amino acid substitutions and indels are implicated in increased transmissibility and enhanced immune evasion. By reverting individual spike mutations of BA.1 or BA.2, we characterize the molecular effects of the Omicron spike mutations on expression, ACE2 receptor affinity, and neutralizing antibody recognition. We identified key mutations enabling escape from neutralizing antibodies at a variety of epitopes. Stabilizing mutations in the N-terminal and S2 domains of the spike protein can compensate for destabilizing mutations in the receptor binding domain, enabling the record number of mutations in Omicron. Our results provide a comprehensive account of the mutational effects in the Omicron spike protein and illustrate previously uncharacterized mechanisms of host evasion.

INTRODUCTION

The continuous evolution and spread of severe acute respiratory syndrome coronavirus 2 (SARS-CoV-2) has produced variants of concern (VOCs) and variants of interest (VOIs) with enhanced immune evasion, transmissibility, and occasionally increased disease severity (Davies et al., 2021; Mlcochova et al., 2021; Saito et al., 2022; Tao et al., 2021; Wang et al., 2021). Omicron (or B.1.1.529) rapidly replaced the Delta VOC globally (Nishiura et al., 2021; Suzuki et al., 2022). The BA.1 sub-lineage of Omicron caused record numbers of infections and breakthrough cases in fully vaccinated and previously infected individuals (Reuters, 2021; Viana et al., 2022). As of February 2022, the BA.2 lineage has replaced BA.1 in many countries and shows additional enhanced transmissibility over all prior VOCs (Cheng et al., 2022; Yamasoba et al., 2022).

The SARS-CoV-2 spike protein is key to both transmissibility and immune evasion (Sette and Crotty, 2021). This homotri-

meric protein is displayed on the SARS-CoV-2 capsid surface, mediates virus binding and entry into host cells, and elicits an immune response that gives rise to neutralizing antibodies and a robust T cell response (GeurtsvanKessel et al., 2022; Grifoni et al., 2021; Moss, 2022). The spike protein ectodomain (ECD) is the primary immune target and consists of three main functional units: the N-terminal domain (NTD), receptor binding domain (RBD), and the fusogenic stalk (S2) (Harvey et al., 2021). Because of its importance in cell entrance and immune escape, spike mutations accumulate in circulating viral variants (Figure 1A). The NTD appears to tolerate the most mutations, harboring 31% of all amino acid (aa) substitutions and 84% of indels found in circulating variants (GISAID database accessed on 18/December/2021) (Figure 1B), whereas the RBD and S2 regions are more restricted in the structural changes that they can tolerate, likely due to conserved functional constraints of host-cell receptor binding and membrane fusion. The functional consequence of these mutations is key for

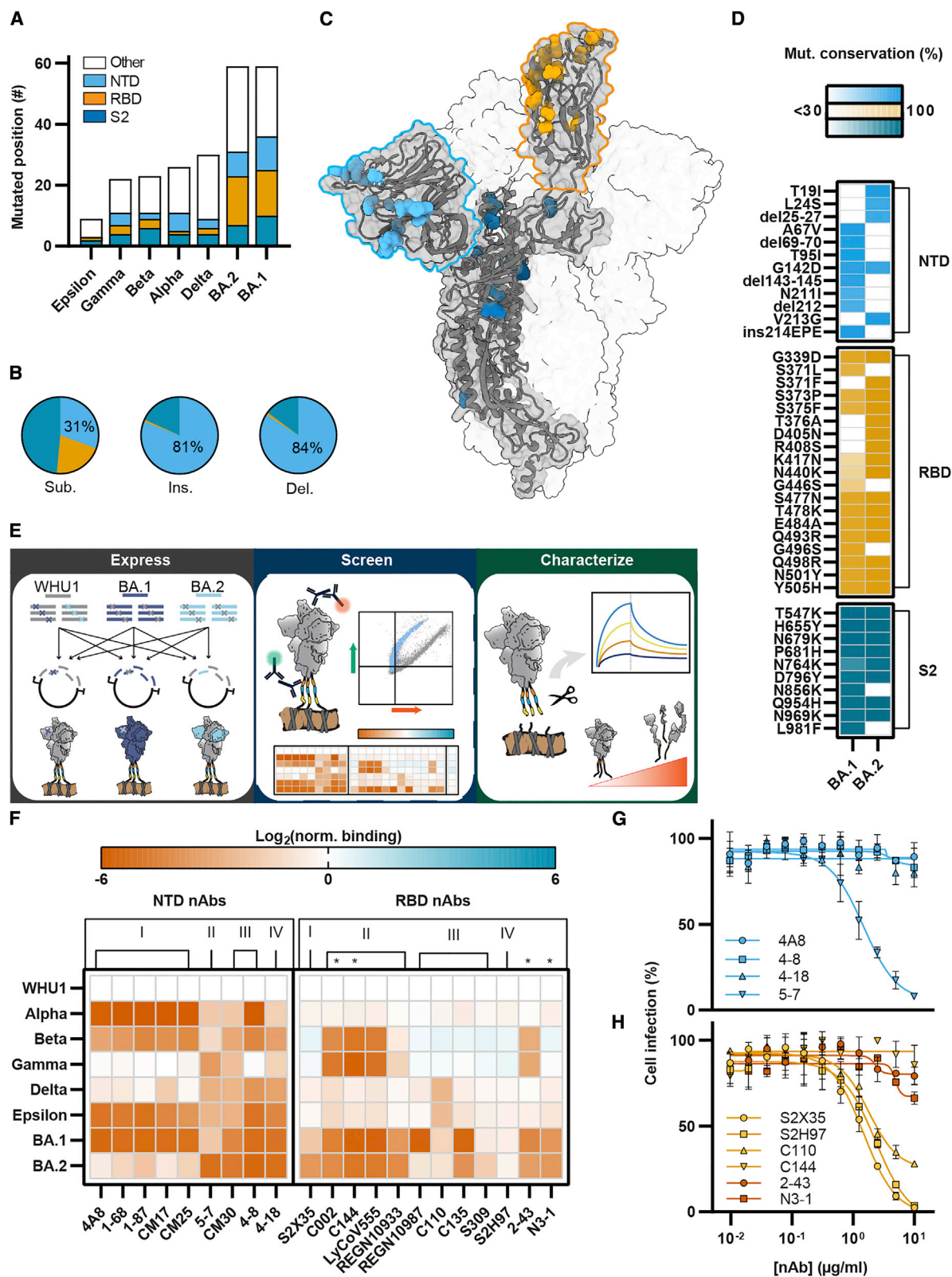


Figure 1. Omicron spike proteins have dozens of mutations contributing antibody escape

(A) The number of mutations (aa) for each VOI and VOC. Spike NTD mutations, light blue; spike RBD mutations, yellow; spike S2 mutations, dark blue; other mutations, white.

(legend continued on next page)

understanding viral evolution and interactions with our immune system.

Omicron BA.1 and BA.2 sub-lineages have an unprecedented 33 and 29 nonsynonymous changes relative to the ancestral Wuhan-Hu-1 (WHU1) lineage. These include four distinct aa deletions (del), one insertion (ins), and 36 substitutions distributed across the ECD (Figure 1C). BA.2 shares 21 of the mutations in BA.1 but also contains eight unique substitutions and dels (Figure 1D). Some of these mutations increase the evasion of neutralizing monoclonal antibodies (mAbs), rendering most mAb therapies ineffective (Cao et al., 2022). Similarly, the mutations reduced authentic virus neutralization by convalescent and vaccinated/boosted sera (Cameroni et al., 2022; Planas et al., 2021). Although recent studies have probed small numbers of individual aa changes within BA.1 and BA.2 (Iketani et al., 2022; Liu et al., 2022), questions about the synergistic and contextual effects of most Omicron mutations remain unanswered.

Here, we leverage mammalian cell surface display of the spike protein to characterize the expression, antibody binding, and cell receptor affinity of coronavirus spike ECDs (Javanmardi et al., 2021). We characterize the effects of all Omicron mutations with respect to human ACE2 (hACE2) binding, spike protein stability, and escape from multiple distinct classes of mAbs. We compare the effects of individual spike protein mutations between the WHU1 and Omicron mutational contexts to reveal how these mutations alter antigenicity and hACE2 affinity. These results also explain how Omicron evades neutralizing mAbs, including those with quaternary binding modes, via changing both the surface epitopes and RBD conformational dynamics. Finally, we show that NTD mutations potentiate new RBD mutations, expanding the ability of the RBD to further evolve under increased evolutionary pressure from adaptive immune responses.

RESULTS

Omicron spike proteins have distinct antigenic features

We used mammalian cell surface display to compare the antigenicity and expression of the BA.1 and BA.2 ECDs (residues 1–1,208) with earlier VOCs (Figure 1E). We transiently expressed spike variants on the surface of mammalian cells (HEK293T) and measured expression, antibody binding, and hACE2 affinity by two-color flow cytometry (Figures S1A and S1B; STAR Methods) (Javanmardi et al., 2021). We first cloned spike proteins from six VOCs (Alpha, Beta, Gamma, Delta, and Omicron BA.1 and BA.2) and one VOI (Epsilon), representing the dominant variants during different surges of the pandemic. The D614G mu-

tation and six prefusion stabilizing prolines were incorporated into all variants to increase surface expression and maintain the prefusion conformation (Hsieh et al., 2020; Korber et al., 2020; Long et al., 2020). We assayed each variant for expression and antibody escape potential with a set of 21 mAbs (Figures 1F, S1C, and S1D) (Barnes et al., 2020; Cerutti et al., 2021b; Chi et al., 2020). Of these, nine are NTD-targeting mAbs (Chi et al., 2020; Liu et al., 2020; Voss et al., 2021), which we previously classified based on their binding epitopes (classes I–IV) (Javanmardi et al., 2021). The remaining 12 target all four classes of neutralizing RBD epitopes (Barnes et al., 2020; Greaney et al., 2021c). We include the clinically used REGN10933 (casirivimab) and REGN10987 (imdevimab) (Hansen et al., 2020; Weinreich et al., 2021, p. 2), LY-CoV555 (bamlanivimab) (Chen et al., 2021), and S309 (sotrovimab) (Gupta et al., 2021; Starr et al., 2021) antibodies. We also tested four mAbs with quaternary RBD binding modes (Barnes et al., 2020;

Goike et al., 2021; Liu et al., 2020) (C002, C144, 2–43, and N3–1) and the pan-variant mAb S2H97 (Goike et al., 2021; Greaney et al., 2021c; Liu et al., 2020; Starr et al., 2021). Together, this panel provides a comprehensive overview of neutralizing antibody escape by variant spike proteins.

Consistent with previous reports (Iketani et al., 2022; Liu et al., 2022; Planas et al., 2021; Yu et al., 2022; Zhou et al., 2022), BA.1 and BA.2 show enhanced antibody escape compared with all other variants (Figure 1F). BA.1 escapes most antibodies in our panel, including nearly all classes of NTD binding mAbs (except class II antibody 5–7). BA.1 spike protein is also refractory to many RBD-targeting mAbs, with strong escape from class II binders, half of the class III binders, and all quaternary binders. BA.2 shows considerable antibody escape but remains susceptible to the class I NTD binders and some class III RBD antibodies. In contrast, BA.2 escapes 5–7, the noncanonical class I RBD binder S2X35, and the class III RBD binder S309 to a greater degree than BA.1. Impressively, RBD targeting mAb S2H97 retained binding for all variants tested, highlighting the therapeutic potential of pan-variant neutralizing antibodies against a continuously evolving virus.

To test whether these results translated to live virus, we performed microneutralization assays with authentic BA.1 virus and a subset of ten mAbs with known neutralization of WHU1. We tested four NTD-binding mAbs, one from each of the four binding classes (Figure 1G). Consistent with the cell surface display results, BA.1 completely escaped neutralization by 4A8 (class I), 4–8 (class III), and 4–18 (class IV). Only the class II mAb 5–7 had a measurable neutralizing effect. Similarly, we tested a representative of each of the four classes of

(B) Distribution of all nonsynonymous mutations (substitutions = 42,077,816; insertions = 31,063; deletions = 15,664,146, colored as in A) found in GISAID (accessed on 18/December/2021). The NTD has the most insertions and deletions (81% and 84%, respectively).

(C) SARS-CoV-2 spike ectodomain structure (PDB: 7DDN; Zhang et al., 2021) with mutations found in BA.1 and BA.2 colored by domain as in (A).

(D) Mutations found in the Omicron spike variants. Shading indicates the percentage of BA.1 or BA.2 strains containing these mutations, as analyzed on outbreak.info (accessed on 12/February/2022).

(E) Spike display platform overview. Spike protein ectodomains are constructed using a semi-automated cloning pipeline, displayed on the surface of HEK293T cells, and assayed with flow cytometry. Biophysical characterization is performed with spikes cleaved from cell surfaces.

(F) Relative mAb binding to spikes from six VOCs and a VOI. Red, decreased binding; blue, increased binding; normalized to the original WHU1 spike with D614G mutation (top row). Mean \pm SD of log-transformed values from at least two biological replicates. Spike domain targets and epitope classifications of antibodies shown on top, *, quaternary binding.

(G and H) Authentic BA.1 virus neutralization for selected NTD- (G) and RBD-directed mAbs. Mean \pm SD of two biological replicates. Curves are a sigmoidal (4PL, X), least squares fit, IC_{50} values listed in Figure S1E.

RBD-targeting mAbs and two additional quaternary binding mAbs (Figure 1H). BA.1 escaped the same antibodies as in the mammalian cell surface display assay. Previous studies reported authentic BA.1 neutralization data for mAbs LyCoV555, REGN10933, REGN10987, and S309 (VanBlargen et al., 2022). In agreement with our cell surface display data, these mAbs completely lost neutralization activity, except for S309, which was minimally affected. In the aggregate, the data showed that our screening method recapitulated other *in vitro* and *in vivo* observations and that the BA.1 and BA.2 spike proteins are antigenically distinct.

BA.1 evades NTD-targeting mAbs better than BA.2

We sought to investigate the molecular mechanism of mAb escape by Omicron, starting with the effects of the NTD mutations (Figure 1F) (McCallum et al., 2021c, 2021a; Wang et al., 2021; Zhou et al., 2021). Compared with previous VOCs, BA.1 and BA.2 have the most mutated NTDs. The BA.1 NTD has four aa substitutions, three dels (del69–del70, del143–del145, and del211) and a novel ins (ins214EPE) (Figure 2A). The BA.2 NTD has four aa substitutions and one del (del25–del27). Several of these mutations are located in the intrinsically disordered NTD-loops (N-loops) that comprise an antigenic supersite (Figures S2A–S2E) (Cerutti et al., 2021b; Javanmardi et al., 2021; McCallum et al., 2021b).

We first screened WHU1 spike protein variants containing each of the individual mutations found in BA.1 and BA.2 (Figure S2F) (Javanmardi et al., 2021). BA.1 completely escaped all NTD class I, III, and IV mAbs due to contiguous mutations (G142D, del143–del145) in the N3-loop (Figures 2B, S2G, and S2H). Binding by 5–7 (class II), which interacts with the periphery of the NTD supersite, was reduced ~5-fold (Cerutti et al., 2021a; Liu et al., 2020). The other BA.1 NTD mutations had moderate effects on binding of 5–7, but the other mAbs were not impacted. BA.2 still retained sensitivity to some NTD-targeting mAbs (Figure 1F). Mutations in the N1-loop (T19I, L24R, and del25–del27) moderately decreased binding for class II, III, and IV mAbs (Figures 2C, S2I, and S2J), and in combination with G142D, BA.2 completely escaped antibody recognition at this site. The V213G substitution was inconsequential for mAb binding in our assays.

Next, we tested whether other BA.1 and BA.2 mutations impacted antibody escape at the NTD. Starting with each of the BA.1 and BA.2 sequences, we reverted each of the NTD mutations to WT and measured the difference in mAb binding when compared with the full variant mutation set (Figures 2D and 2E). Reversion of the N3-loop mutations in BA.1 fully restored binding for all the affected mAbs (Figure 2F). However, reversion of the del211, L212I, and ins214EPE mutation cluster failed to restore binding by 5–7 to WHU1 levels. Reversion of N1-loop mutations and G142D in the BA.2 context each partially restored binding, showing the additive effect of antibody escape for the class II, III, and IV mAbs (Figure 2G). Reversion of T19I in the BA.2 context failed to restore any binding for mAb CM30, due to the strong escape elicited by the other BA.2 NTD mutations. Thus, BA.1 and BA.2 effectively evade class III and IV mAbs but show different binding of class I and II mAbs. These observations highlight the continued immunological selection to evade potent NTD-targeting mAbs (Harvey et al., 2021; McCallum et al., 2021b).

Mutation context of Omicron RBDs impact mAb escape mechanisms

Despite the significance of immunologic responses to the NTD, mucosal and systemic responses to SARS-CoV-2 infection primarily target the RBD during the acute phase of infection (Greaney et al., 2021a, 2021b; Piccoli et al., 2020). Thus, understanding the molecular mechanisms underlying RBD-targeting mAb escape is crucial. BA.1 and BA.2 share 12 RBD substitutions, with three additional substitutions (S371L, G446S, and G496S) unique to BA.1 and four substitutions (S371F, T376A, D405N, and R408S) unique to BA.2 (Figure 3A). To study the effects of these RBD substitutions on mAb binding, we first screened WHU1 spike protein variants containing each of the individual mutations found in BA.1 and BA.2 (Figures 3B and S3A). S2X35, a class I mAb, showed moderately reduced binding due to the E484A mutation. However, each of the S371F, D405N, and R408S substitutions caused substantial decreases in binding, likely accounting for enhanced resistance of BA.2 to S2X35. Class II antibodies and the quaternary binder 2–43 were most affected by the E484A and Q493R single mutations. Class III mAb REGN10987 showed decreased binding with both the N440K and G446S single mutations, and C135 binding was greatly affected by both N440K and Q498R (Figure 3B). Two other class III mAbs, C110 and S309, were weakly affected by S371F and were not escaped by the Omicron spike proteins. S2H97, a class IV mAb, had 4.3-fold decreased binding due to the S371F substitution, versus the 1.4-fold decrease observed with the full set of BA.2 spike mutations. Conversely, no individual substitution greatly reduced N3–1 binding despite the strong binding escape observed within the full Omicron spike proteins.

Previous studies of Omicron mutations on mAb escape have been performed by adding Omicron mutations to the WHU1 spike protein (Iketani et al., 2022; Liu et al., 2022). These binding or escape measurements fail to capture the nonadditive, epistatic interactions among the mutated sites (Rochman et al., 2022; Starr et al., 2022). To explore these contextual effects, we reverted each individual Omicron RBD mutation back to the WT aa in the corresponding BA.1 and BA.2 spike proteins and assayed binding (Figures 3C and 3D). Reversions associated with improved binding, relative to the full set of Omicron mutations, were interpreted to be important for escape in BA.1 or BA.2. In the BA.2, no single reversion restored S2X35 binding, suggesting an additive effect of S371F, D405N, and R408S mutations. LyCoV555 appeared to escape by contributions from E484A and Q493R. REGN10933 binding was greatly restored by both S477N and Q493R reversion in BA.1 and BA.2. The K417N reversion substantially restored mAb binding for the BA.1 spike protein but not BA.2. REGN10987 retained affinity to BA.2 due to the absence of the G446S substitution and dampened sensitivity to N440K in the BA.2 context. C135's escape in BA.2 appears driven by N440K, which completely restored binding when reverted. In BA.1, reverting N440K, G446S, and N501Y all restored binding, suggesting that they all contribute to escape. No reversion in either Omicron context fully restored binding for the quaternary mAbs C144 or 2–43. Finally, N3–1 binding improved upon reverting S375F in the BA.1 spike and, to a lesser degree, S373P in BA.2. Although these individual mutations do not directly clash with the N3–1 Fabs in the WHU1 structure, there are likely direct or allosteric perturbations to

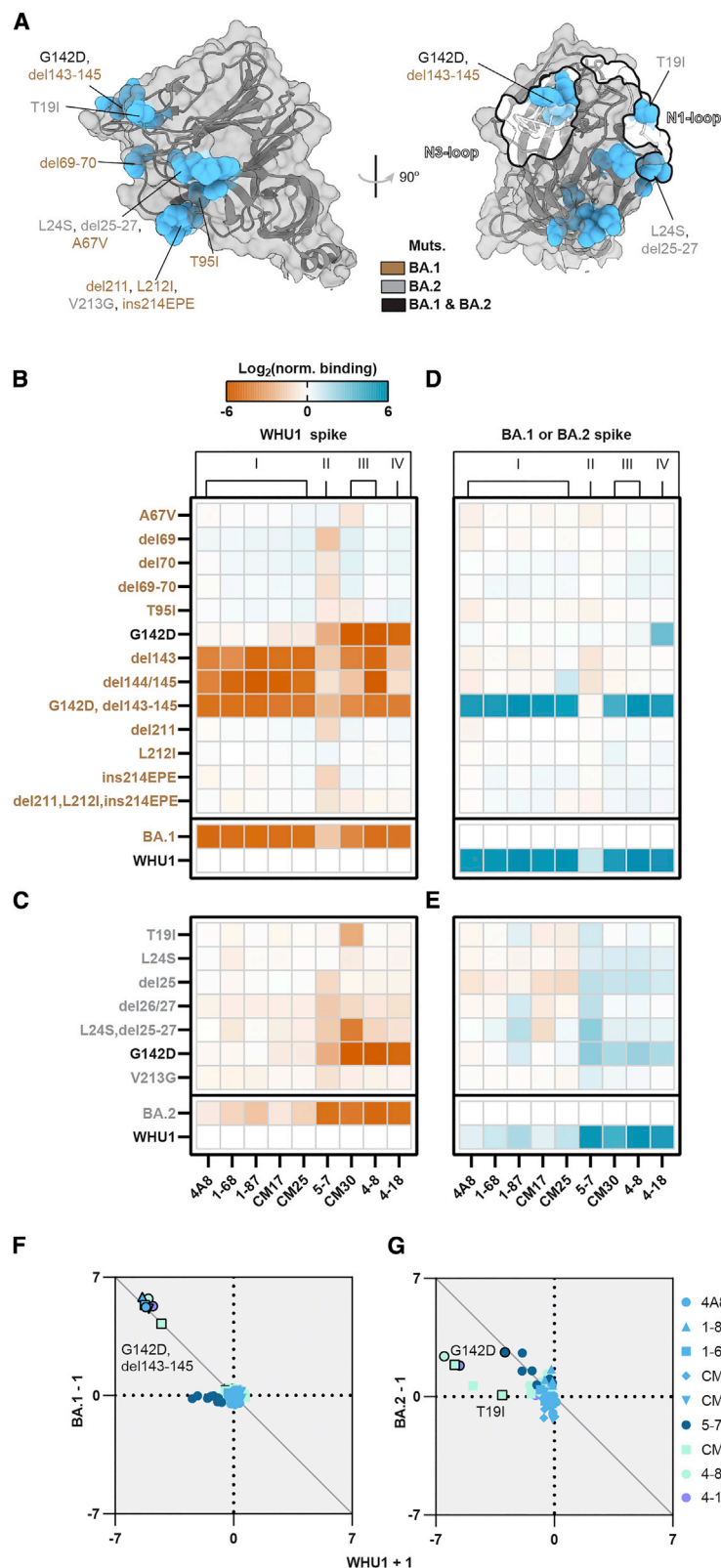


Figure 2. NTD indels and substitutions enable mAb binding escape

(A) An enlarged NTD structure (PDB: 7DDN; Zhang et al., 2021) with nonsynonymous mutations from BA.1 (brown), BA.2 (gray), or both (black) indicated.

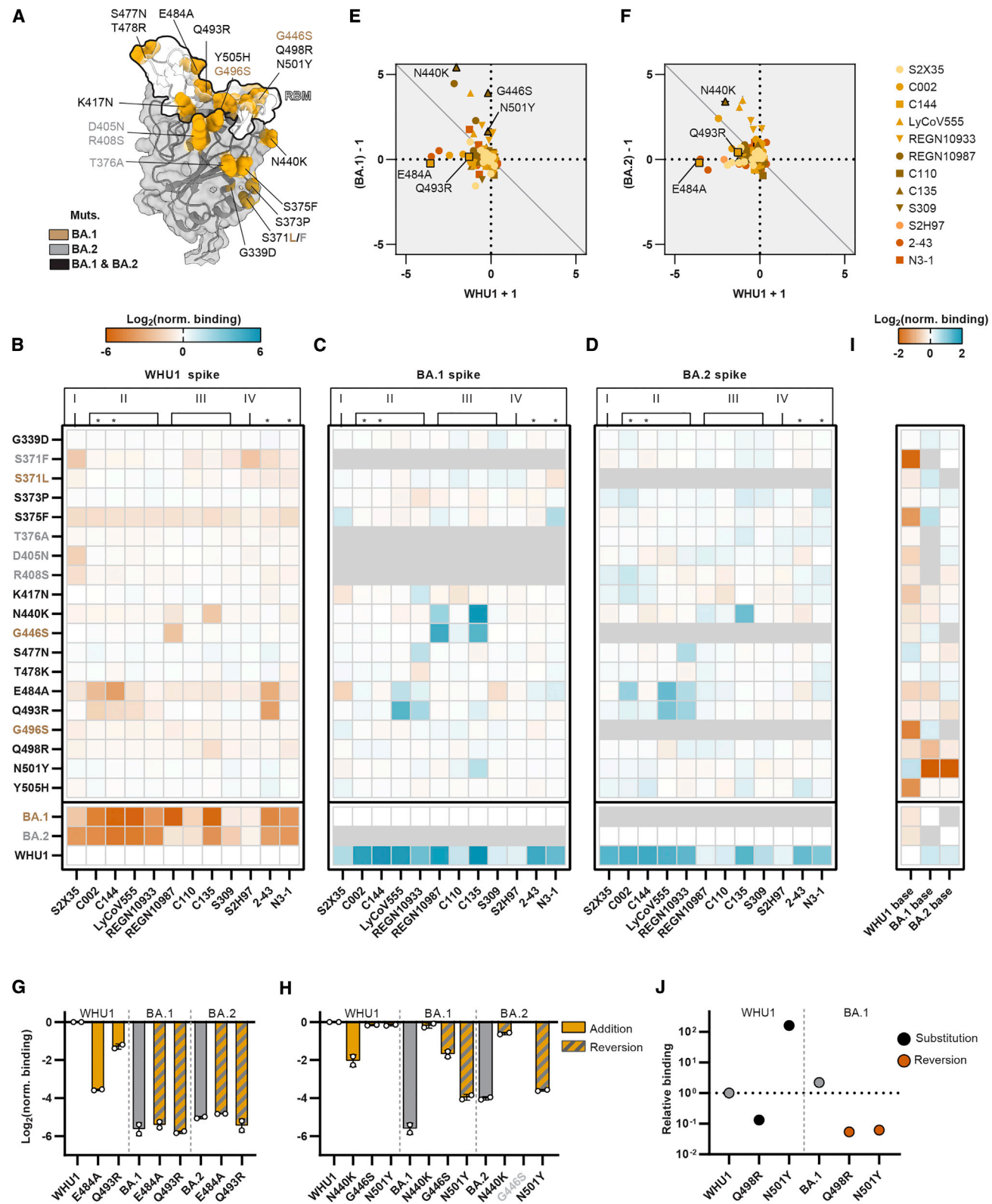
(B and C) Relative mAb binding to WHU1 spike proteins containing BA.1-NTD (B) or BA.2-NTD (C) mutations. Red, decreased binding; blue, increased binding; normalized to the WHU1 spike. Mutations color coded as in (A).

(D and E) Relative mAb binding to BA.1 (D) or BA.2 (E) spike proteins containing reversions of the respective BA.1- or BA.2-NTD mutations to the WHU1 sequence. Colored as in B, normalized to the BA.1 (D) or BA.2 (E) spike.

(F) Comparison of \log_2 (normalized binding) measurements for adding (+1) BA.1-NTD mutations to the WHU1 spike versus reverting (−1) the corresponding mutations from the BA.1 spike protein. Mutations with equal antigenic effects in both spike contexts are expected to fall on the diagonal line $y = -x$.

(G) Comparison of the effect of adding and reverting BA.2-NTD mutations as in (F).

For all plots, mean \pm SD of log-transformed values from at least two biological replicates.



(legend on next page)

N3-1's engagement of the Omicron spike (Figure S3B), highlighting the importance of context in studying antibody escape pathways.

When comparing the effects of adding and reverting mutations in different contexts, two interesting cases emerge: (1) mutations that are sufficient for escape in the WHU1 spike but not necessary in the BA.1 or BA.2 spikes and (2) mutations that are insufficient for escape by the WHU1 spike but necessary for the BA.1 or BA.2 spikes (Figures 3E and 3F). Sufficient but not necessary mutations (below the diagonal line) may indicate examples where BA.1 or BA.2 have stacked multiple mutations that each break a mAb-spike protein binding interaction. For example, C144 binding was strongly disrupted by either E484A or Q493R when these mutations were made to the WHU1 spike but reverting E484A in the BA.1 or BA.2 spike failed to restore binding (Figure 3G). Necessary but not sufficient mutations (above the diagonal line) may indicate mutational clusters that have a synergistic or epistatic effect on antibody binding. As an example, N440K reduced, and G446S and N501Y slightly reduced the binding of antibody C135 when made in the WHU1 context (Figure 3H). BA.1, which has these three mutations, nearly eliminated C135 binding, and this binding was partially restored when any of the three mutations are reverted. The restoration effect from BA.1 is considerably larger than the reduction in binding from WHU1 suggesting that N440K, G446S, and N501Y have synergistic effects greater than their individual effects. In contrast, BA.2, which lacks G446S, does not show such clear synergy between N440K and N501Y. Overall, these results highlight antigenic differences between the BA.1 and BA.2.

BA.1 and BA.2 RBDs balance antibody escape and ACE2 binding

Nearly half of the BA.1 and BA.2 RBD mutations are in the receptor binding motif (RBM). We screened each single RBD aa substitution in the WHU1 spike protein and observed increased hACE2 binding with the S477N and N501Y mutations (Figure 3I). Conversely, mutations S371F, S375F, G496S, and Y505H decreased hACE2 affinity. These results are consistent with previously reported RBD deep mutational scanning (DMS) measurements (Starr et al., 2020), although S371F was more detrimental to binding in our assay. Structural studies of BA.2 reveal enhanced

interprotomer RBD-RBD packing due to the hydrophobic residue substitutions in the 371–376 loop, relative to the WHU1 spike protein (Stalls et al., 2022). Thus, we posit that S371F detrimentally affects hACE2 affinity through RBD conformational changes that are only measurable in the context of a full spike glycoprotein.

Reverting each individual RBD mutation showed that the deleterious effects of S371F, S375F, K417N, Q496S, and Y505H on hACE2 binding to be less severe in the Omicron contexts. The critical role of N501Y for hACE2 binding by Omicron spikes was also shown, as its removal nearly abrogated hACE2 binding (Figures 3I, S3D, and S3E). Although Q498R reduced hACE2 binding in the WHU1 context, it improved hACE2 binding for the BA.1 spike and, to a lesser extent, the BA.2 spike. Cooperative hACE2 binding due to the Q498R and N501Y substitutions has been previously noted, but the mutation-specific effects had not been measured in the full BA.1 and BA.2 spike proteins (Starr et al., 2022; Zahradnik et al., 2021). We validated these results via biolayer interferometry (BLI) using dimeric hACE2 (Figures 3J and S3H). Together, these results highlight the starkly different molecular basis for hACE2 engagement for BA.1 and BA.2, and the importance of the spike genetic context in understanding these interactions (Cerutti et al., 2022; McCallum et al., 2022; Yin et al., 2021).

Cryptic cross-domain interactions in the BA.1 spike contribute to mAb escape

Reversion of single RBD mutations in Omicron spikes broadly failed to fully restore mAbs with quaternary binding modes (C002, C144, 2-43, N3-1) (Figures S3F and S3G). These mAbs simultaneously engage two or three RBDs to enhance their binding. We reasoned that these antibodies do not bind Omicron relative to the WHU1 spike because of changes in the RBD conformation dynamics. In support of this hypothesis, structures of the BA.1 spike revealed a strict 1-RBD-up and 2-RBD-down conformation (Cerutti et al., 2022). To identify potential cross-domain interactions that may contribute to the extent of escape measured for the full set of BA.1 and BA.2 spike mutations, we created variants containing combinations of NTD, RBD, and S2 mutation sets from the WHU1, BA.1 or BA.2 variants. We assayed these spike proteins for mAb binding using 12 RBD-targeting mAbs (Figure 4A). For most RBD-targeting mAbs, such as C144, the set of BA.1- and BA.2-RBD mutations alone

Figure 3. Omicron-RBD mutations enable antibody evasion and preserve hACE2 affinity

- (A) An enlarged RBD structure (PDB: 7DDN; Zhang et al., 2021) with mutations in BA.1 (brown), BA.2 (gray), or both (black) indicated.
- (B) Relative monoclonal antibody binding to WHU1 spike proteins containing BA.1- and BA.2-RBD mutations. Red, decreased binding; blue, increased binding; relative to the WHU1 spike.
- (C and D) Relative monoclonal antibody binding to BA.1 (C) or BA.2 (D) spike proteins containing reversions of the respective BA.1- or BA.2-RBD mutations to the WHU1 sequence. Colored as in B, normalized to the BA.1 (C) or BA.2 (D) spike.
- (E) Comparison of the effect of adding (+1) BA.1-RBD mutations to the WHU1 spike protein versus reverting (−1) the corresponding mutations from the BA.1 spike. Mutations with equal antigenic effects in both spike contexts are expected to fall on the diagonal line $y = -x$.
- (F) Comparison of the effect of adding and reverting BA.2-RBD mutations as in (E).
- (G and H) Relative mAb C144 (G) or C135 (H) binding to the WHU1, BA.1, and BA.2 spike proteins and spike proteins containing the indicated substitutions or reversions as appropriate, normalized to the level of binding to the WHU1 spike.
- (I) Relative monomeric hACE2 binding to WHU1 spikes containing BA.1- and BA.2-RBD mutations (WHU1 base), and BA.1/BA.2 spike proteins containing reversions of the BA.1- or BA.2-RBD mutations (BA.1 base/BA.2 base). Red, decreased binding; blue, increased binding; relative to the WHU1, BA.1, and BA.2 spike proteins as appropriate.
- (J) Monomeric hACE2 binding to WHU1 and BA.1 spike proteins and variants containing substitutions or reversions as appropriate, measured by BLI. All values are normalized to the binding of the WHU1 spike.
- For all plots, mean \pm SD of log-transformed values from at least two biological replicates.

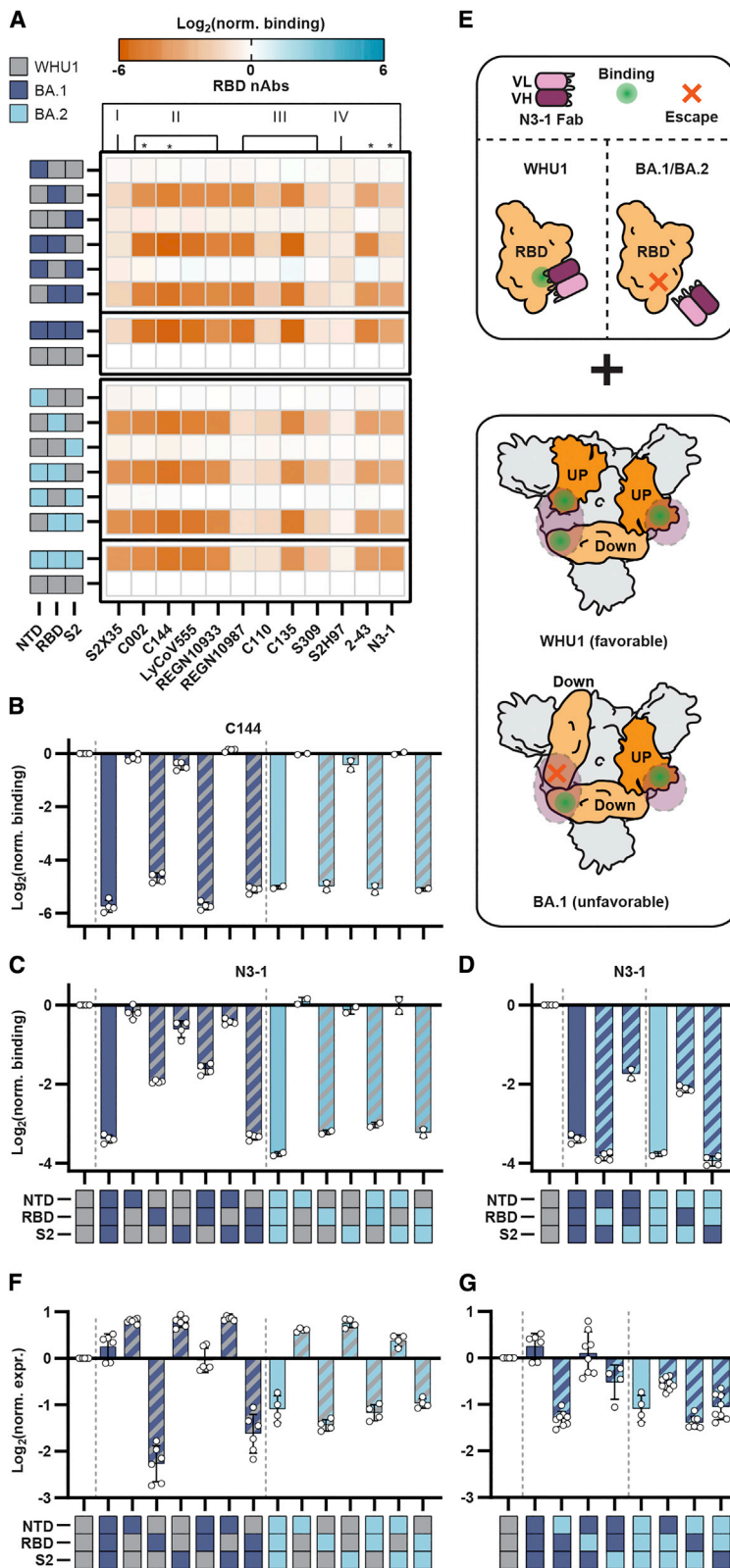


Figure 4. Cross-domain interactions contribute to mAb escape and stabilize the Omicron spike protein

(A) Differences in monoclonal antibody binding of RBD-directed antibodies against spike proteins containing combinations of the NTD, RBD, and S2 mutation sets from the BA.1 and BA.2 variants. Red, decreased binding; blue, increased binding, relative to the WHU1 spike.

(B and C) Relative mAb C144 (B) or N3-1 (C) binding to spike proteins containing combinations of the NTD, RBD, and S2 BA.1 and BA.2 mutation sets relative to WHU1.

(D) Additional N3-1 binding data as in (C).

(E) Proposed escape mechanism for biparatropic antibody (N3-1) by Omicron spike proteins. Antibody binding reduced via mutations at the N3-1 binding epitope on the RBD (top). Top-down view of spike protein trimers with annotated RBD up versus down positions (bottom). Violet circles, N3-1 binding epitope.

(F) Differences in expression of spike proteins containing combinations of the NTD, RBD, and S2 BA.1 and BA.2 mutation sets. Data normalized to WHU1 spike expression.

(G) Additional expression data as in (F).

For all plots, mean \pm SD of log-transformed values from at least two biological replicates.

decreased binding to the level of the complete set Omicron mutations (Figure 4B). Interestingly, only the combination of BA.1-RBD and -S2 mutations recapitulate the loss of N3-1 binding measured for the full BA.1 spike (Figure 4C). In contrast, the BA.2-RBD mutations alone were adequate for reduced N3-1 binding.

To determine if differences in BA.1 and BA.2 escape of N3-1 were intrinsic to RBD and S2 mutations, we created chimeric spikes by swapping BA.1 and BA.2 mutation sets (NTD, RBD, and S2) (Figure 4D). We observed a further 1.4-fold reduction in N3-1 binding when the BA.1-RBD was replaced with the BA.2-RBD. Furthermore, the BA.2-S2 mutations did not synergistically reduce N3-1 binding when combined with the BA.1-NTD and -RBD mutations. Conversely, replacing BA.2-RBD mutations with BA.1-RBD mutations dampened N3-1 escape. By swapping the BA.1-S2 mutations into the BA.2 spike, we did observe a marginal (1.1-fold) reduction in N3-1 binding. We postulate that the N856K and L981F mutations, which comprise the only differences between the BA.1- and BA.2-S2 mutations sets, alter the RBD-up vs -down equilibrium or spike conformation, thus further reducing N3-1 binding. These data highlight possible routes of quaternary-binding mAb evasion by Omicron through altering antigenic epitopes and RBD dynamics (Figure 4E).

Omicron spike domains provide stability compensation to immune evasive RBD

Expression correlates with improved infectivity and viral fitness (Gobeil et al., 2021; Meng et al., 2021). BA.1 spikes express 1.2-fold greater than WHU1 spikes, whereas BA.2 express 2.1-fold lower (Figure S1D). We determined the combination of mutations responsible for this increased expression by establishing the effect of each individual Omicron mutation. Spike expression was monitored from two discrete epitopes: a triple FLAG in the linker between the ECD and transmembrane domain and the foldon trimerization domain (Figures S4A and S4B; STAR Methods). Most of the BA.1 and BA.2 NTD and S2 mutations enhanced spike expression. For example, NTD mutations del69-del70 and ins214EPE in BA.1 and G142D shared by both BA.1 and BA.2 improved WHU1 spike expression. Reversion of either del69-del70 or ins214EPE in the BA.1 spike only modestly decreased expression (Figure S4C). Interestingly, the G142D mutation is more central to the overall stability of the BA.2 spike, as its reversion reduced expression 5.3-fold. We also observed extremely destabilizing mutations in the BA.1 and BA.2 RBDs. The addition of S375F to the WHU1 spike dramatically reduced expression 12-fold. Mutations N440K and E484A, which are responsible for mAb escape, and N501Y, which enhances hACE2 affinity are also mildly destabilizing (Figure S4D).

Next, we assayed each set of domain-specific mutations in the context of WHU1 spike to determine their relative effects on spike expression (Figure 4F). We found that both the BA.1- and BA.2-RBD mutation sets greatly reduced spike protein expression relative to WHU1, whereas the NTD and S2 mutation sets increased expression. The fully mutated BA.1 spike had greater expression than the WHU1 spike, suggesting that the destabilizing mutations in the RBD are compensated for primarily by mutations in the NTD and S2 domains. Further domain exchanges showed that the BA.1 NTD mutations are sufficient to stabilize

the BA.1 RBD mutations, with the S2 mutations contributing, but insufficient on their own. BA.2 follows the same general pattern; however, the BA.2-NTD and -S2 were less effective at offsetting the relatively milder decreased expression associated with the BA.2-RBD. This finding is consistent with the relatively poor spike expression in BA.2, compared with expression in WHU1 and BA.1. Finally, we swapped BA.1 and BA.2 domains to determine if stabilizing effects were transferrable. Interestingly, the exchange of BA.2 NTD mutations into the BA.1 spike greatly reduce spike expression (Figure 4G). The exchange of BA.1 RBD mutations into the BA.2 spike also reduced BA.2 spike expression.

To test how expression relates to spike stability, we analyzed the thermal denaturation of a subset of spike variants via differential scanning fluorimetry (DSF) (STAR Methods). Soluble spike trimers generate two distinct denaturation peaks, denoted here as Tm1 and Tm2. Compared with other VOCs, the BA.1 and BA.2 spike proteins have poor thermostability, as shown by their respective 7°C and 6°C shifts in Tm1, relative to WHU1 (Figure S5A). DSF measurements reveal that these effects are driven by RBD mutations in BA.1 (Figures S5B and S5C) and BA.2 (Figures S5D and S5E) in agreement with a recent study that showed similar Tm shifts for the purified, monomeric RBD proteins (BA.1 = 7°C, BA.2 = 4°C) (Stalls et al., 2022). BA.1 and BA.2 spikes are destabilized by their highly mutated RBDs. Although the BA.1 NTD mutations do not improve the thermostability of the spike protein, they compensate for poor spike expression. Taken together, these results reveal that the expression loss due to mAb-evasive, destabilizing RBD mutations are offset by otherwise stabilizing NTD and S2 mutations. These mutations work synergistically with a particular spike background, as swapping mutation sets between BA.1 and BA.2 leads to overall reduced expression.

DISCUSSION

This work dissects the effects of individual mutations in different spike protein contexts to understand how these mutations evade neutralizing antibodies and impact expression or stability. In contrast to the NTD, mutations in Omicron RBDs often resulted in nonadditive levels of escape from RBD-targeting mAbs. We identified instances where multiple mutations were required to escape binding completely. For example, reversions of either N440K or G446S in the BA.1 spike largely restored the binding of REGN10933 and C135 (Figure 3C). We also identified several class II mAbs (C002 and C144) that failed to show binding improvements after single mutation reversions in the Omicron spike proteins, suggesting redundant mutations contributing to antigenic escape (Figures 3B–3D). We speculate that Omicron RBDs have undergone extensive mutation under continuous pressure to evade diverse classes of RBD-targeting antibodies, outside of the predominant class II antibodies found in polyclonal plasmas after immunization or natural infection (Greaney et al., 2021c). This redundancy in escape may also arise from mutation-induced alterations in RBD conformational equilibria and dynamics, as described in prior structural studies (Cerutti et al., 2022; McCallum et al., 2022; Stalls et al., 2022).

Reverting individual BA.1 and BA.2 mutations back to WT (WHU1) generally failed to restore binding for the four mAbs

with quaternary binding modes (Figures S3F and S3G). These results suggested that the virus was not simply presenting different epitopes but presenting them in differing conformational states. We showed that RBD-S2 cross-domain interactions in the BA.1 spike led to reduced N3-1 binding beyond the BA.1-RBD mutations alone (Figure 4C). Furthermore, the removal of the N856K and L981F mutations from the BA.1 spike, which are implicated in creating cross-domain interactions, partially restored N3-1 binding to the level of the BA.1-RBD mutations (Figure 4D). Similarly, BA.2-RBD mutations proved even more effective than BA.1-RBD mutations for escaping N3-1, in line with recently solved structures that show that the down conformation of the RBD is largely stabilized in the BA.2-RBD mutations (Stalls et al., 2022).

The accumulation of novel mutation clusters in Omicron came at the cost of destabilizing the RBD. Several RBD mutations, most notably S375F, drastically reduce spike expression (Figure S4D). We propose that NTD mutations such as the 69-70 del offset protein folding/stability deficiencies associated with Omicron RBDs (Meng et al., 2021). Addition of BA.1-NTD mutations compensated for the poor expression of the BA.1-RBD mutations (Figure 4F). However, the same compensation effects were not seen with the BA.2-NTD and BA.2-RBD mutations, resulting in a lower net expression of BA.2 spike relative to WHU1. Importantly, two new sub-lineages of Omicron, BA.4 and BA.5, which differ from the BA.2 spike by a few mutations (del69–del70, L452R, F486V, and R493Q), are gradually replacing the previously dominant BA.2 variant, globally. This could be due to the reappearance of the 69–70 del, which likely improves the BA.4/BA.5 spike stability/expression relative to the BA.2 spike, providing a fitness advantage. Future studies will be required to explore whether and how improvements in immune evasion have led to fitness costs for Omicron relative to spike expression and fitness.

Our data suggest that the Omicron BA.1 and BA.2 subvariants retain high affinity for hACE2. Previous directed evolution (Zahradnik et al., 2021) and yeast surface display (YSD)-DMS (Starr et al., 2022) studies have shown N501Y to greatly improve hACE2 binding and Q498R to moderately reduce it; these studies also determined that the co-occurrence of N501Y and Q498R synergistically boosted hACE2 affinity. We confirm that the full Omicron BA.1 and BA.2 spikes also benefit from these substitutions, with N501Y and Q498R playing critical roles in the molecular engagement of hACE2 (Figures 3I and 3J). Taken together, these results reveal evolutionary features of Omicron that enable the accrual of immune evasive mutations without sacrificing hACE2 affinity and infectivity.

This work also informs on several design principles for future antibody and vaccine development. Our results highlight the efficacy of mAbs previously shown to have high-affinity spike binding and moderate degrees of sarbecovirus breadth, such as S309 and S2H97 (Starr et al., 2021). Both mAbs remain resistant to escape from all six of the VOCs we assayed, including BA.1 and BA.2. These findings support the approach of using spike epitope features, such as mutational constraint to prioritize therapeutic antibodies (Starr et al., 2021, 2020). However, our data also reveal mechanisms for SARS-CoV-2 to bypass mutational constraints and evade antibodies by modifying structural dynamics. Thus, simply using BA.1 or BA.2 spike immunogens in

next generation SARS-CoV-2 vaccines will likely fail to provide long-term protection against future VOCs.

Our study has several limitations. First, we used a prefusion stabilized spike protein that does not precisely mimic the dynamics of the native Omicron spike protein (Hsieh et al., 2020). Second, our binding assays use a set of potent neutralizing mAbs which only serve as proxies for the antibodies found in patient antibody repertoires after immunization or natural infection. Third, our work only touches on antibody recognition and hACE2 binding; T cell immunity plays a critical role in protecting against SARS-CoV-2 disease. Additional studies focused on the perturbations of spike variants on T cell response will continue to bridge the gap in the understanding of immune escape between humoral and cell-mediated immunity.

In the aggregate, the data presented here add critical information about key features of Omicron spike protein mutations and how these mutations synergize to successfully evade antibodies while maintaining high-affinity hACE2 binding. Our binding maps largely complement structure-based studies of binding escape but now provide insights into the role of compensatory substitutions in the NTD that impact both expression/stability and conformation. We conclude that the continuing accumulation of NTD mutations will further alter the conformational equilibrium and stability of the spike protein to allow for the accumulation of new, more virulent mutations in the RBD. As SARS-CoV-2 continues to evolve and new variants arise and spread, it is critical that these mutations can be understood in their native genetic contexts to better inform future antibody and vaccine development campaigns. Finally, mammalian cell display will continue to serve as a powerful platform for investigating evolutionary trajectories of infectious agents and engineering conformational vaccine candidates.

STAR★METHODS

Detailed methods are provided in the online version of this paper and include the following:

- KEY RESOURCES TABLE
- RESOURCE AVAILABILITY
 - Lead Contact
 - Materials Availability
 - Data and Code Availability
- EXPERIMENTAL MODEL AND SUBJECT DETAILS
- METHOD DETAILS
 - Automated pipeline for spike variant cloning
 - Expression and purification of neutralizing anti-spike monoclonal antibodies
 - Expression and purification of chimeric ACE2-Fc
 - Expression and purification of SARS-CoV-2 spike proteins
 - HEK293T transfection
 - Flow cytometry and data analysis
 - SARS-COV-2 authentic virus neutralization assay
 - Biolayer Interferometry
 - Differential Scanning Fluorimetry
 - Computational analysis of GISAID sequence data
 - Structural analyses and data visualization
- QUANTIFICATION AND STATISTICAL ANALYSIS

SUPPLEMENTAL INFORMATION

Supplemental information can be found online at <https://doi.org/10.1016/j.chom.2022.07.016>.

ACKNOWLEDGMENTS

We thank Dr. Sasha M. Pejerrey, Dr. Heather McConnell, and Ms. Adrienne Winston for editorial contributions. The research was supported in part by the Houston Methodist Academic Institute Infectious Diseases Fund and many generous Houston philanthropists (J.M.M. and J.D.G.). We are grateful to Carole Walter Looke and Jim Looke for their generous philanthropic gift to ADAPT (J.D.G.). The funders had no role in the design and conduct of the study; collection, management, analysis, and interpretation of the data; preparation, review, or approval of the manuscript; and decision to submit the manuscript for publication. K.J. was supported by the Provost's Graduate Excellence Fellowship (PGEF) at UT Austin. C.D.J. was supported by the P2P-TEAM Program (1T32GM139796-01). The research was also supported by a Cooperative Agreement (W911NF-17-2-0091) between ARL and UT Austin to A.D.E. and J.D.G., the Bill and Melinda Gates Foundation (K.J., C.-W.C., A.A., and I.J.F.), and the Welch Foundation (F-1808 to I.J.F., F-1655 to A.D.E.).

AUTHOR CONTRIBUTIONS

K.J., T.H.S.-S., I.J.F., and J.D.G. designed the research. K.J. performed the flow experiments. K.J., D.R.B., A.A., and J.D.G. purified antibodies and other reagents. K.J. and T.H.S.-S. cloned spike variants. K.J. and C.-W.C. performed BLI and DSF experiments. R.J.O. and J.M.M. isolated and sequenced Omicron. X.X., H.X., P.-Y.S., and S.W. provided the authentic virus neutralization data. K.J., T.H.S.-S., C.D.J., and J.D.G. analyzed the data. K.J., T.H.S.-S., A.D.E., I.J.F., and J.D.G. wrote the paper with editorial assistance from all co-authors.

DECLARATION OF INTERESTS

D.R.B., A.D.E., and J.D.G. have filed patent applications monoclonal antibodies targeting SARS-CoV-2. K.J., C.-W.C., and I.J.F. have filed patent applications on spike 6p (HexaPro).

INCLUSION AND DIVERSITY

One or more of the authors of this paper self-identifies as an underrepresented ethnic minority in science. The author list of this paper includes contributors from the location where the research was conducted who participated in the data collection, design, analysis, and/or interpretation of the work.

Received: April 21, 2022

Revised: June 17, 2022

Accepted: July 27, 2022

Published: August 4, 2022

REFERENCES

- Barnes, C.O., Jette, C.A., Abernathy, M.E., Dam, K.-M.A., Esswein, S.R., Gristick, H.B., Malyutin, A.G., Sharaf, N.G., Huey-Tubman, K.E., Lee, Y.E., et al. (2020). SARS-CoV-2 neutralizing antibody structures inform therapeutic strategies. *Nature* 588, 682–687. <https://doi.org/10.1038/s41586-020-2852-1>.
- Cameroni, E., Bowen, J.E., Rosen, L.E., Saliba, C., Zepeda, S.K., Culap, K., Pinto, D., VanBlargan, L.A., De Marco, A., di Iulio, J., et al. (2022). Broadly neutralizing antibodies overcome SARS-CoV-2 Omicron antigenic shift. *Nature* 602, 664–670. <https://doi.org/10.1038/s41586-021-04386-2>.
- Cao, L., Goreshnik, I., Coventry, B., Case, J.B., Miller, L., Kozodoy, L., Chen, R.E., Carter, L., Walls, A.C., Park, Y.-J., et al. (2020). De novo design of picomolar SARS-CoV-2 miniprotein inhibitors. *Science* 370, 426–431. <https://doi.org/10.1126/science.abd9909>.
- Cao, Y., Wang, J., Jian, F., Xiao, T., Song, W., Yisimayi, A., Huang, W., Li, Q., Wang, P., An, R., et al. (2022). Omicron escapes the majority of existing SARS-

CoV-2 neutralizing antibodies. *Nature* 602, 657–663. <https://doi.org/10.1038/s41586-021-04385-3>.

Cerutti, G., Guo, Y., Liu, L., Liu, L., Zhang, Z., Luo, Y., Huang, Y., Wang, H.H., Ho, D.D., Sheng, Z., and Shapiro, L. (2022). Cryo-EM structure of the SARS-CoV-2 Omicron spike. *Cell Rep.* 38, 110428. <https://doi.org/10.1016/j.celrep.2022.110428>.

Cerutti, G., Guo, Y., Wang, P., Nair, M.S., Wang, M., Huang, Y., Yu, J., Liu, L., Katsamba, P.S., Bahna, F., et al. (2021a). Neutralizing antibody 5-7 defines a distinct site of vulnerability in SARS-CoV-2 spike N-terminal domain. *Cell Rep* 37, 109928. <https://doi.org/10.1016/j.celrep.2021.109928>.

Cerutti, G., Guo, Y., Zhou, T., Gorman, J., Lee, M., Rapp, M., Reddem, E.R., Yu, J., Bahna, F., Bimela, J., et al. (2021b). Potent SARS-CoV-2 neutralizing antibodies directed against spike N-terminal domain target a single Supersite. *Cell Host Microbe* 29, 819–833.e7. <https://doi.org/10.1016/j.chom.2021.03.005>.

Chen, P., Nirula, A., Heller, B., Gottlieb, R.L., Boscia, J., Morris, J., Huhn, G., Cardona, J., Mocherla, B., Stosor, V., et al. (2021). SARS-CoV-2 neutralizing antibody LY-CoV555 in outpatients with Covid-19. *N. Engl. J. Med.* 384, 229–237. <https://doi.org/10.1056/NEJMoa2029849>.

Cheng, V.C.-C., Ip, J.D., Chu, A.W.-H., Tam, A.R., Chan, W.-M., Abdullah, S.M.U., Chan, B.P.-C., Wong, S.-C., Kwan, M.Y.-W., Chua, G.T., et al. (2022). Rapid spread of SARS-CoV-2 Omicron subvariant BA.2 in a single-source community outbreak. *Clin. Infect. Dis.* ciac203. <https://doi.org/10.1093/cid/ciac203>.

Chi, X., Yan, R., Zhang, J., Zhang, G., Zhang, Y., Hao, M., Zhang, Z., Fan, P., Dong, Y., Yang, Y., et al. (2020). A neutralizing human antibody binds to the N-terminal domain of the Spike protein of SARS-CoV-2. *Science* 369, 650–655. <https://doi.org/10.1126/science.abc6952>.

Davies, N.G., Abbott, S., Barnard, R.C., Jarvis, C.I., Kucharski, A.J., Munday, J.D., Pearson, C.A.B., Russell, T.W., Tully, D.C., Washburne, A.D., et al. (2021). Estimated transmissibility and impact of SARS-CoV-2 lineage B.1.1.7 in England. *Science* 372, eabg3055. <https://doi.org/10.1126/science.abg3055>.

GeurtsvanKessel, C.H., Geers, D., Schmitz, K.S., Mykityn, A.Z., Lamers, M.M., Bogers, S., Scherbeijn, S., Gommers, L., Sablerolles, R.S.G., Nieuwkoop, N.N., et al. (2022). Divergent SARS-CoV-2 Omicron-reactive T and B cell responses in COVID-19 vaccine recipients. *Sci. Immunol.* 7, eabo2202. <https://doi.org/10.1126/sciimmunol.abo2202>.

Gobeil, S.M.-C., Janowska, K., McDowell, S., Mansouri, K., Parks, R., Manne, K., Stalls, V., Kopp, M.F., Henderson, R., Edwards, R.J., et al. (2021). D614G mutation alters SARS-CoV-2 spike conformation and enhances protease cleavage at the S1/S2 junction. *Cell Rep.* 34, 108630. <https://doi.org/10.1016/j.celrep.2020.108630>.

Goike, J., Hsieh, C.-L., Horton, A., Gardner, E.C., Bartzoka, F., Wang, N., Javanmardi, K., Herbert, A., Abbassi, S., Renberg, R., et al. (2021). Synthetic repertoires derived from convalescent COVID-19 patients enable discovery of SARS-CoV-2 neutralizing antibodies and a novel quaternary binding modality. Preprint at bioRxiv. <https://doi.org/10.1101/2021.04.07.438849>.

Greaney, A.J., Loes, A.N., Crawford, K.H.D., Starr, T.N., Malone, K.D., Chu, H.Y., and Bloom, J.D. (2021a). Comprehensive mapping of mutations in the SARS-CoV-2 receptor-binding domain that affect recognition by polyclonal human plasma antibodies. *Cell Host Microbe* 29, 463–476.e6. <https://doi.org/10.1016/j.chom.2021.02.003>.

Greaney, A.J., Loes, A.N., Gentles, L.E., Crawford, K.H.D., Starr, T.N., Malone, K.D., Chu, H.Y., and Bloom, J.D. (2021b). Antibodies elicited by mRNA-1273 vaccination bind more broadly to the receptor binding domain than do those from SARS-CoV-2 infection. *Sci. Transl. Med.* 13, eabi9915. <https://doi.org/10.1126/scitranslmed.abi9915>.

Greaney, A.J., Starr, T.N., Barnes, C.O., Weisblum, Y., Schmidt, F., Caskey, M., Gaebler, C., Cho, A., Agudelo, M., Finkin, S., et al. (2021c). Mapping mutations to the SARS-CoV-2 RBD that escape binding by different classes of antibodies. *Nat. Commun.* 12, 4196. <https://doi.org/10.1038/s41467-021-24435-8>.

Grifoni, A., Sidney, J., Vita, R., Peters, B., Crotty, S., Weiskopf, D., and Sette, A. (2021). SARS-CoV-2 human T cell epitopes: adaptive immune response

against COVID-19. *Cell Host Microbe* 29, 1076–1092. <https://doi.org/10.1016/j.chom.2021.05.010>.

Gupta, A., Gonzalez-Rojas, Y., Juarez, E., Crespo Casal, M., Moya, J., Falci, D.R., Sarkis, E., Solis, J., Zheng, H., Scott, N., et al. (2021). Early treatment for Covid-19 with SARS-CoV-2 neutralizing antibody sotrovimab. *N. Engl. J. Med.* 385, 1941–1950. <https://doi.org/10.1056/NEJMoa2107934>.

Hansen, J., Baum, A., Pascal, K.E., Russo, V., Giordano, S., Wloga, E., Fulton, B.O., Yan, Y., Koon, K., Patel, K., et al. (2020). Studies in humanized mice and convalescent humans yield a SARS-CoV-2 antibody cocktail. *Science* 369, 1010–1014. <https://doi.org/10.1126/science.abd0827>.

Harvey, W.T., Carabelli, A.M., Jackson, B., Gupta, R.K., Thomson, E.C., Harrison, E.M., Ludden, C., Reeve, R., Rambaut, A., et al.; COVID-19 Genomics UK (COG-UK) Consortium (2021). SARS-CoV-2 variants, spike mutations and immune escape. *Nat. Rev. Microbiol.* 19, 409–424. <https://doi.org/10.1038/s41579-021-00573-0>.

Hsieh, C.-L., Goldsmith, J.A., Schaub, J.M., DiVenere, A.M., Kuo, H.-C., Javanmardi, K., Le, K.C., Wrapp, D., Lee, A.G., Liu, Y., et al. (2020). Structure-based design of prefusion-stabilized SARS-CoV-2 spikes. *Science* 369, 1501–1505. <https://doi.org/10.1126/science.abd0826>.

Iketani, S., Liu, L., Guo, Y., Liu, L., Chan, J.F., Huang, Y., Wang, M., Luo, Y., Yu, J., Chu, H., et al. (2022). Antibody evasion properties of SARS-CoV-2 Omicron sublineages. *Nature* 604, 553–556. <https://doi.org/10.1038/s41586-022-04594-4>.

Javanmardi, K., Chou, C.-W., Terrace, C.I., Annapareddy, A., Kaoud, T.S., Guo, Q., Lutgens, J., Zorkic, H., Horton, A.P., Gardner, E.C., et al. (2021). Rapid characterization of spike variants via mammalian cell surface display. *Mol. Cell* 81, 5099–5111.e8. <https://doi.org/10.1016/j.molcel.2021.11.024>.

Korber, B., Fischer, W.M., Gnanakaran, S., Yoon, H., Theiler, J., Abfalterer, W., Hengartner, N., Giorgi, E.E., Bhattacharya, T., Foley, B., et al. (2020). Tracking changes in SARS-CoV-2 spike: evidence that D614G increases infectivity of the COVID-19 virus. *Cell* 182, 812–827.e19. <https://doi.org/10.1016/j.cell.2020.06.043>.

Liu, L., Wang, P., Nair, M.S., Yu, J., Rapp, M., Wang, Q., Luo, Y., Chan, J.F.-W., Sahi, V., Figueroa, A., et al. (2020). Potent neutralizing antibodies against multiple epitopes on SARS-CoV-2 spike. *Nature* 584, 450–456. <https://doi.org/10.1038/s41586-020-2571-7>.

Liu, L., Iketani, S., Guo, Y., Chan, J.F., Wang, M., Liu, L., Luo, Y., Chu, H., Huang, Y., Nair, M.S., et al. (2022). Striking antibody evasion manifested by the Omicron variant of SARS-CoV-2. *Nature* 602, 676–681. <https://doi.org/10.1038/s41586-021-04388-0>.

Long, S.W., Olsen, R.J., Christensen, P.A., Bernard, D.W., Davis, J.J., Shukla, M., Nguyen, M., Saavedra, M.O., Yerramilli, P., Pruitt, L., et al. (2020). Molecular architecture of early dissemination and massive second wave of the SARS-CoV-2 virus in a major metropolitan area. *mBio* 11, e02707–20. <https://doi.org/10.1128/mBio.02707-20>.

McCallum, M., Bassi, J., De Marco, A., Chen, A., Walls, A.C., Di Iulio, J., Tortorici, M.A., Navarro, M.-J., Silacci-Fregni, C., Saliba, C., et al. (2021a). SARS-CoV-2 immune evasion by the B.1.427/B.1.429 variant of concern. *Science* 373, 648–654. <https://doi.org/10.1126/science.abi7994>.

McCallum, M., Czudnochowski, N., Rosen, L.E., Zepeda, S.K., Bowen, J.E., Walls, A.C., Hauser, K., Joshi, A., Stewart, C., Dillen, J.R., et al. (2022). Structural basis of SARS-CoV-2 Omicron immune evasion and receptor engagement. *Science* 375, 864–868.

McCallum, M., De Marco, A.D., Lempp, F.A., Tortorici, M.A., Pinto, D., Walls, A.C., Beltramello, M., Chen, A., Liu, Z., Zatta, F., et al. (2021b). N-terminal domain antigenic mapping reveals a site of vulnerability for SARS-CoV-2. *Cell* 184, 2332–2347.e16. <https://doi.org/10.1016/j.cell.2021.03.028>.

McCallum, M., Walls, A.C., Sprouse, K.R., Bowen, J.E., Rosen, L.E., Dang, H.V., De Marco, A., Franko, N., Tilles, S.W., Logue, J., et al. (2021c). Molecular basis of immune evasion by the Delta and Kappa SARS-CoV-2 variants. *Science* 374, 1621–1626. <https://doi.org/10.1126/science.abl8506>.

Meng, B., Kemp, S.A., Papa, G., Datir, R., Ferreira, I.A.T.M., Marelli, S., Harvey, W.T., Lytras, S., Mohamed, A., Gallo, G., et al. (2021). Recurrent emergence of SARS-CoV-2 spike deletion H69/V70 and its role in the Alpha variant B.1.1.7. *Cell Rep.* 35, 109292. <https://doi.org/10.1016/j.celrep.2021.109292>.

Micochova, P., Kemp, S.A., Dhar, M.S., Papa, G., Meng, B., Ferreira, I.A.T.M., Datir, R., Collier, D.A., Albecka, A., Singh, S., et al. (2021). SARS-CoV-2 B.1.617.2 Delta variant replication and immune evasion. *Nature* 599, 114–119. <https://doi.org/10.1038/s41586-021-03944-y>.

Moss, P. (2022). The T cell immune response against SARS-CoV-2. *Nat. Immunol.* 23, 186–193. <https://doi.org/10.1038/s41590-021-01122-w>.

Nishiura, H., Ito, K., Anzai, A., Kobayashi, T., Piantam, C., and Rodríguez-Morales, A.J. (2021). Relative reproduction number of SARS-CoV-2 Omicron (B.1.1.529) compared with Delta variant in South Africa. *J. Clin. Med.* 11, 30. <https://doi.org/10.3390/jcm11010030>.

Piccoli, L., Park, Y.-J., Tortorici, M.A., Czudnochowski, N., Walls, A.C., Beltramello, M., Silacci-Fregni, C., Pinto, D., Rosen, L.E., Bowen, J.E., et al. (2020). Mapping neutralizing and immunodominant sites on the SARS-CoV-2 spike receptor-binding domain by structure-guided high-resolution serology. *Cell* 183, 1024–1042.e21. <https://doi.org/10.1016/j.cell.2020.09.037>.

Planas, D., Saunders, N., Maes, P., Guivel-Benhassine, F., Planchais, C., Buchrieser, J., Bolland, W.-H., Porrot, F., Staropoli, I., Lemoine, F., et al. (2021). Considerable escape of SARS-CoV-2 Omicron to antibody neutralization. *Nature* 602, 671–675. <https://doi.org/10.1038/d41586-021-03827-2>.

Reuters. (2021). WHO says Omicron in 89 countries and spreading rapidly. *The Guardian* 18, 2021. <https://www.theguardian.com/world/2021/dec/18/who-says-omicron-in-89-countries-and-spreading-rapidly>.

Rochman, N.D., Faure, G., Wolf, Y.I., Freddolino, P.L., Zhang, F., and Koonin, E.V. (2022). Epistasis at the SARS-CoV-2 receptor-binding domain interface and the propitiously boring implications for vaccine escape. *mBio* 13, e00135–22. <https://doi.org/10.1128/mbio.00135-22>.

Saito, A., Irie, T., Suzuki, R., Maemura, T., Nasser, H., Uriu, K., Kosugi, Y., Shirakawa, K., Sadamasu, K., Kimura, I., et al. (2022). Enhanced fusogenicity and pathogenicity of SARS-CoV-2 Delta P681R mutation. *Nature* 602, 300–306. <https://doi.org/10.1038/s41586-021-04266-9>.

Sette, A., and Crotty, S. (2021). Adaptive immunity to SARS-CoV-2 and COVID-19. *Cell* 184, 861–880. <https://doi.org/10.1016/j.cell.2021.01.007>.

Stalls, V., Lindenberger, J., Gobeil, S.M.-C., Henderson, R., Parks, R., Barr, M., Deyton, M., Martin, M., Janowska, K., Huang, X., et al. (2022). Cryo-EM structures of SARS-CoV-2 Omicron BA.2 spike. *Cell Rep.* 39, 111009. <https://doi.org/10.1016/j.celrep.2022.111009>.

Starr, T.N., Czudnochowski, N., Liu, Z., Zatta, F., Park, Y.-J., Addetia, A., Pinto, D., Beltramello, M., Hernandez, P., Greaney, A.J., et al. (2021). SARS-CoV-2 RBD antibodies that maximize breadth and resistance to escape. *Nature* 597, 97–102. <https://doi.org/10.1038/s41586-021-03807-6>.

Starr, T.N., Greaney, A.J., Hannon, W.W., Loes, A.N., Hauser, K., Dillen, J.R., Ferri, E., Farrell, A.G., Dadonaite, B., McCallum, M., et al. (2022). Shifting mutational constraints in the SARS-CoV-2 receptor-binding domain during viral evolution. *Science* 377, 420–424. <https://doi.org/10.1126/science.abo7896>.

Starr, T.N., Greaney, A.J., Hilton, S.K., Ellis, D., Crawford, K.H.D., Dingens, A.S., Navarro, M.J., Bowen, J.E., Tortorici, M.A., Walls, A.C., et al. (2020). Deep mutational scanning of SARS-CoV-2 receptor binding domain reveals constraints on folding and ACE2 binding. *Cell* 182, 1295–1310.e20. <https://doi.org/10.1016/j.cell.2020.08.012>.

Suzuki, R., Yamasoba, D., Kimura, I., Wang, L., Kishimoto, M., Ito, J., Morioka, Y., Nao, N., Nasser, H., Uriu, K., et al. (2022). Attenuated fusogenicity and pathogenicity of SARS-CoV-2 Omicron variant. *Nature* 603, 700–705. <https://doi.org/10.1038/s41586-022-04462-1>.

Tao, K., Tzou, P.L., Nouhin, J., Gupta, R.K., de Oliveira, T., Kosakovsky Pond, S.L., Fera, D., and Shafer, R.W. (2021). The biological and clinical significance of emerging SARS-CoV-2 variants. *Nat. Rev. Genet.* 22, 757–773. <https://doi.org/10.1038/s41576-021-00408-x>.

VanBlargan, L.A., Errico, J.M., Halfmann, P.J., Zost, S.J., Crowe, J.E., Purcell, L.A., Kawaoka, Y., Corti, D., Fremont, D.H., and Diamond, M.S. (2022). An infectious SARS-CoV-2 B.1.1.529 Omicron virus escapes neutralization by therapeutic monoclonal antibodies. *Nat. Med.* 28, 490–495. <https://doi.org/10.1038/s41591-021-01678-y>.

- Viana, R., Moyo, S., Amoako, D.G., Tegally, H., Scheepers, C., Althaus, C.L., Anyaneji, U.J., Bester, P.A., Boni, M.F., Chand, M., et al. (2022). Rapid epidemic expansion of the SARS-CoV-2 Omicron variant in southern Africa. *Nature* 603, 679–686. <https://doi.org/10.1038/s41586-022-04411-y>.
- Voss, W.N., Hou, Y.J., Johnson, N.V., Delidakis, G., Kim, J.E., Javanmardi, K., Horton, A.P., Bartzoka, F., Paresi, C.J., Tanno, Y., et al. (2021). Prevalent, protective, and convergent IgG recognition of SARS-CoV-2 non-RBD spike epitopes. *Science* 372, 1108–1112. <https://doi.org/10.1126/science.abg5268>.
- Wang, P., Nair, M.S., Liu, L., Iketani, S., Luo, Y., Guo, Y., Wang, M., Yu, J., Zhang, B., Kwong, P.D., et al. (2021). Antibody resistance of SARS-CoV-2 variants B.1.351 and B.1.1.7. *Nature* 593, 130–135. <https://doi.org/10.1038/s41586-021-03398-2>.
- Weinreich, D.M., Sivapalasingam, S., Norton, T., Ali, S., Gao, H., Bhoire, R., Musser, B.J., Soo, Y., Rofail, D., Im, J., et al. (2021). REGN-COV2, a neutralizing antibody cocktail, in outpatients with Covid-19. *N. Engl. J. Med.* 384, 238–251. <https://doi.org/10.1056/NEJMoa2035002>.
- Wrapp, D., Wang, N., Corbett, K.S., Goldsmith, J.A., Hsieh, C.L., Abiona, O., Graham, B.S., and McLellan, J.S. (2020). Cryo-EM structure of the 2019-nCoV spike in the prefusion conformation. *Science* 367, 1260–1263. <https://doi.org/10.1126/science.abb2507>.
- Xie, X., Lokugamage, K.G., Zhang, X., Vu, M.N., Muruato, A.E., Menachery, V.D., and Shi, P.Y. (2021). Engineering SARS-CoV-2 using a reverse genetic system. *Nat. Protoc.* 16, 1761–1784. <https://doi.org/10.1038/s41596-021-00491-8>.
- Yamasoba, D., Kimura, I., Nasser, H., Morioka, Y., Nao, N., Ito, J., Uriu, K., Tsuda, M., Zahradnik, J., Shirakawa, K., et al. (2022). Virological characteristics of SARS-CoV-2 BA.2 variant. *Cell* 185, 2103–2115.e19. <https://doi.org/10.1016/j.cell.2022.02.14.480335>.
- Yin, W., Xu, Y., Xu, P., Cao, X., Wu, C., Gu, C., He, X., Wang, X., Huang, S., Yuan, Q., et al. (2021). Structures of the Omicron spike trimer with ACE2 and an anti-Omicron antibody. *Science* 375, 1048–1053. <https://doi.org/10.1101/2021.12.27.474273>.
- Yu, J., Collier, A.Y., Rowe, M., Mardas, F., Ventura, J.D., Wan, H., Miller, J., Powers, O., Chung, B., Siamatu, M., et al. (2022). Neutralization of the SARS-CoV-2 omicron BA.1 and BA.2 variants. *N. Engl. J. Med.* 386, 1579–1580. <https://doi.org/10.1056/NEJMc2201849>.
- Zahradnik, J., Marciano, S., Shemesh, M., Zoler, E., Harari, D., Chiaravalli, J., Meyer, B., Rudich, Y., Li, C., Marton, I., et al. (2021). SARS-CoV-2 variant prediction and antiviral drug design are enabled by RBD in vitro evolution. *Nat. Microbiol.* 6, 1188–1198. <https://doi.org/10.1038/s41564-021-00954-4>.
- Zhang, C., Wang, Y., Zhu, Y., Liu, C., Gu, C., Xu, S., Wang, Y., Zhou, Y., Wang, Y., Han, W., et al. (2021). Development and structural basis of a two-MAB cocktail for treating SARS-CoV-2 infections. *Nat. Commun.* 12, 264. <https://doi.org/10.1038/s41467-020-20465-w>.
- Zhou, D., Dejnirattisai, W., Supasa, P., Liu, C., Mentzer, A.J., Ginn, H.M., Zhao, Y., Duyvesteyn, H.M.E., Tuekprakhon, A., Nutalai, R., et al. (2021). Evidence of escape of SARS-CoV-2 variant B.1.351 from natural and vaccine-induced sera. *Cell* 184, 2348–2361.e6. <https://doi.org/10.1016/j.cell.2021.02.037>.
- Zhou, H., Tada, T., Dcosta, B.M., and Landau, N.R. (2022). Neutralization of SARS-CoV-2 Omicron BA.2 by therapeutic monoclonal antibodies. Preprint at bioRxiv. <https://doi.org/10.1101/2022.02.15.480166>.
- Zou, J., Kurhade, C., Xia, H., Liu, M., Xie, X., Ren, P., and Shi, P.-Y. (2022). Cross-neutralization of Omicron BA.1 against BA.2 and BA.3 SARS-CoV-2. *Nat. Commun.* 13, 2956. <https://doi.org/10.1038/s41467-022-30580-5>.

STAR★METHODS

KEY RESOURCES TABLE

REAGENT or RESOURCE	SOURCE	IDENTIFIER
Antibodies		
Mouse anti-FLAG M2	Sigma-Aldrich	Cat# F3165; RRID:AB_259529
Goat anti-Mouse IgG(H+L), Human ads-Alexa Fluor 488	Southern Biotech	Cat# 1031-30; RRID:AB_2794315
Goat anti-Human IgG Fc-Alexa Fluor 647	Southern Biotech	Cat# 2048-31; RRID:AB_2795692
Biological samples/viruses		
SARS-CoV-2 virus		strain USA-WA1-2020
Bacterial strains		
Mix & Go Competent Cells - Strain Zymo 10B	Zymo Research	T3019
Chemicals, peptides, and recombinant proteins		
Superior Broth	AthenaES	0105
Expi293 Expression Medium	Gibco	A1435102
DMEM, high glucose, pyruvate	Gibco	11995065
Fetal Bovine Serum	Gibco	26140079
Opti-MEM I Reduced Serum Medium, GlutaMAX Supplement	Gibco	51985091
Penicillin-Streptomycin (5,000 U/mL)	Gibco	15070063
Lipofectamine 3000 Transfection Reagent	Invitrogen	L3000015
Bovine Serum Albumin	Sigma-Aldrich	A3294
5X SYPRO Orange Protein Gel Stain	Supelco	S5692
Surfactant P20	Cytiva	BR100054
Commercial kits and enzymes		
T7 DNA Ligase	NEB	M0318S
AarI (2 U/μL)	Thermo Fisher	ER1582
T4 DNA Ligase	NEB	B0202S
Promega Wizard SV 96 Plasmid DNA Purification Kit	Promega	A2250
ExpiFectamine 293 Transfection Kit	Gibco	A14525
Mycoplasma Detection Kit	Southern Biotech	13100-01
Pierce HRV 3C Protease Solution Kit	Thermo Fisher	88946
Deposited data		
Spike Display data	This paper	Data S1
Experimental models: Cell lines		
HEK293T	ATCC	CRL-3216; RRID:CVCL_0063
Vero E6	ATCC	CRL-1586; RRID:CVCL_0574
Expi293F Cells	Thermo Fisher	A14527; RRID:CVCL_D615
Oligonucleotides		
Synthetic DNA (eBlocks) for cloning	Integrated DNA Technologies	NA
Recombinant DNA		
SARS-CoV-2 S HexaPro	Hsieh et al., 2020	Addgene #154754
Spike Display Part Spacers	Javanmardi et al., 2021	Addgene #172727-172733
Spike Display DO	Javanmardi et al., 2021	Addgene #172721-172726
Software and algorithms		
FlowJo v9	BD	NA

(Continued on next page)

Continued

REAGENT or RESOURCE	SOURCE	IDENTIFIER
SA3800 Spectral Cell Analyzer Software	SONY	NA
MATLAB (2021b)	MathWorks	https://matlab.mathworks.com/
ChimeraX 1.1	UCSF	https://www.cgl.ucsf.edu/chimerax/download.html
GraphPad Prism 9	GraphPad	https://www.graphpad.com/scientific-software/prism/
Octet Data Analysis software (v11.1)	FortéBio	NA

Public datasets

Antibody binding data	Javanmardi et al., 2021	Data S1 ("Binding" tab)
-----------------------	---	-------------------------

Other

384-well Echo Source Plate	Biolab	PP-0200
96-well Clear Round Bottom 2.2 mL Polypropylene Deep Well Plate (Sterile)	Axygen	P-2ML-SQ-C-S
Protein G magnetic beads	Promega	G7471
Protein A Agarose	Thermo Fisher	15918014
Strep-Tactin Superflow resin	IBA	2-1206-025
Superose 6 increase 10/300	GE healthcare	GE29-0915-96
Cell Culture Dishes (10 cm)	VWR	10062-880
Cell Culture Plate (6-well)	VWR	10861-696
Cell Culture Plate (12-well)	VWR	10861-698
96-well qPCR plate	Corning	AXYPCR96LC480WNF
black, μ CLEAR flat-bottom 96-well plate	Greiner Bio-One	655096
LUNA-II Automated Cell Counter	Logos biosystems	L40002
SA3800 Spectral Analyzer	SONY	NA
Echo 525 Acoustic Liquid Handler	Beckman Coulter	NA
Tecan Fluent robotic liquid handler	Tecan	NA
Roche LightCycler 480 II	Roche	NA
Octet Anti-Mouse Fc Capture (AMC) Biosensors	FortéBio	18-5088
Octet RED96e	FortéBio	NA
QPix 420 Colony Picker	Molecular Devices	NA
Cytation 7	BioTek	NA
Detailed bench protocols for Spike Display assays	Javanmardi et al., 2021	Methods S1 in Javanmardi et al., 2021

RESOURCE AVAILABILITY

Lead Contact

Further information and reasonable requests for resources and reagents should be directed to and will be fulfilled by the lead contact, Jimmy D. Gollihar (ggollihar2@houstonmethodist.org).

Materials Availability

Plasmids generated in this study may be provided by the lead contact upon reasonable request.

This study did not generate new cell lines or antibodies.

Data and Code Availability

- This paper analyzes existing, publicly available data from previous publications. Datasets are listed in the [key resources table](#).
- This paper does not report original code. All programs used to analyze GISAID data are freely available online (see [key resources table](#)).
- Any additional information required to reanalyze the data reported in this paper is available from the lead contact upon reasonable request.

EXPERIMENTAL MODEL AND SUBJECT DETAILS

HEK293T (ATCC CRL-3216) cells were cultured in media containing DMEM (Gibco 11995065), phenol red, 4 mM L-glutamine, 110 mg L⁻¹ sodium pyruvate, 4.5 g L⁻¹ D-glucose, and supplemented with 10% FBS (Gibco 26140079) and 2% Pen/Strep (Gibco 15070063). Cells were maintained in a humidified atmosphere of 5% CO₂ and 37 °C and were passaged regularly (2-3 days) into 10 cm polystyrene coated plates (VWR 10062-880) once high cell density was reached. Cells lines were also tested for mycoplasma contamination before use via the Mycoplasma Detection Kit (SouthernBiotech 13100-01).

METHOD DETAILS

Automated pipeline for spike variant cloning

We used a high-throughput automated cloning pipeline that includes an Echo 525 (Beckman Coulter) acoustic liquid handler, a Tecan Fluent robotic liquid handler (Tecan), and the QPix 420 Colony Picker (Molecular Devices) to assemble Golden Gate constructs.

We arranged parts, either IDT eBlocks or plasmids (Addgene 172727-172733), compatible with Golden Gate assembly in a 384-well Echo Source Plate (PP-0200) and transferred parts into 96-well PCR destination plates using an Echo 525 liquid handler. To each well, we added the following Golden Gate reaction mixture: 0.25 µL of T7 DNA Ligase (NEB M0318S), 0.25 µL of AarI (Thermo Fisher ER1582), 0.2 µL AarI Oligo (Thermo Fisher), 1 µL T4 DNA Ligase Buffer (NEB B0202S), 1 µL of each part (eBlock or plasmid), 1 µL of sfGFP-DO destination vector (Addgene 172721-172726), and nuclease-free water to bring the final volume to 10 µL per reaction.

We incubated the reaction mixtures on a thermocycler using the following settings: 25 digestion and ligation cycles (1 min at 37°C and 2 min at 16°C), a final digestion step (30 min at 37°C), and heat inactivation (20 min at 80°C). For assemblies with 4+ parts, we increased the cycled digestion and ligation steps to 3 and 5 min, respectively, to improve assembly efficiencies.

To allow high-throughput transfers to be performed using multichannel pipettes or the Tecan Fluent, we prepared 96-well PCR plates containing 50 µL of Zymo DH10β Mix & Go Competent Cells (prepared using Zymo T3019) per well. To transform the cells, we transferred 4 µL from each unique reaction mixture to corresponding wells containing 50 µL of the Mix & Go Competent Cells. We mixed the wells using gentle pipetting and then incubated cells at 4°C for 10 min. We then transferred the DNA-cell mixtures to a deep well grow block (Axygen P-2ML-SQ-C-S) containing 150 µL of Superior Broth (AthenaES 0105) per well before incubation at 37°C on a plate shaker set to 950 rpm for 1 h.

We plated outgrown cells dropwise onto Nunc OmniTrays (5 µL per spot) (Thermo Fisher 140156). The trays contained 100 µg mL⁻¹ of LB agar + carbenicillin and each plate could hold ninety-six 5-µL drops. We allowed the drops to dry at room temperature before transferring the plates to an incubator at 37°C for 12-16 h for growth overnight.

The next day, we screened and picked colonies using the QPix 420 (Molecular Devices). We selected only white colonies and avoided green fluorescent colonies, which contained the sfGFP cassette but not the spike sequence. We picked the colonies into Axygen deep well grow blocks containing 1 mL of Superior Broth (SB) media + carbenicillin (100 µg/mL) and grew them overnight at 37°C with shaking. Once the colonies were established, we used a 3000 g, 10-min centrifugation step to pellet the liquid cultures and then used the Tecan Fluent robotic liquid handler with Promega Wizard SV 96 Plasmid DNA Purification Kit (Promega A2250) for miniprep. We used Sanger sequencing to verify each plasmid.

Expression and purification of neutralizing anti-spike monoclonal antibodies

We cultured Expi293 cells (Thermo Fisher A14527) in Expi293 Expression Medium (Gibco A1435102) and used a humidified cell culture incubator to maintain cells at 37°C and 8% CO₂ with continuous shaking at 125 rpm. For transfection, we used an ExpiFectamine 293 Transfection Kit (Gibco A14525) according to the manufacturer's instructions. Briefly, we transfected cells with VH and VL expression vectors at a 1:3 molar ratio. Five days after transfection, we collected the protein-containing supernatant using a two-step centrifugation protocol. First, we separated cells and supernatant by centrifuging cultures at 4°C and 300 g for 5 min. Next, we separated cell debris and supernatant by centrifuging at 4°C and 3,000 g for 25 min. To purify human IgGs, we washed Protein G magnetic beads (Promega G7471) with PBS buffer and added the beads to the separated supernatant in a 1:10 volumetric ratio. After a 1h incubation with gyration at room temperature, we used a magnetic peg stand to pellet bead-bound antibodies, which we washed before final elution with a 100 mM glycine-HCl solution at pH 2.5. Finally, we passed the elute through a 0.22-µm syringe filter to clarify residual beads before neutralization with 2 M Tris buffer at pH 7.5. We kept purified antibodies at 4°C or -20°C for short and long-term storage, respectively.

Expression and purification of chimeric ACE2-Fc

We recombinantly expressed human ACE2-Fc in Expi293 cells (Thermo Fisher A14527) using a previously described method with minor modification (Wrapp et al., 2020). Briefly, we transfected the ACE2-Fc expression vector into Expi293T cells using the ExpiFectamine 293 Transfection Kit (Gibco A14525). Five days after transfection, we centrifuged the cultures at 4°C and 300 g for 5 min and collected the supernatant. We further separated cell debris and supernatant by centrifuging at 10,000 g and 4°C for 20 min. After resuspending it in PBS, we purified ACE2-Fc over Protein A Agarose (Thermo Fisher 15918014). We next equilibrated the Protein A Agarose in PBS buffer, ran through the supernatant three times, and used 10 bed volumes of PBS buffer for washing.

Finally, we used 100 mM glycine-HCl at pH 2.4 to elute ACE2-Fc into 0.1x volume Tris buffer at pH 8.5 and 100 mM NaCl. We kept purified ACE2-Fc at 4°C and -20°C for short and long-term storage, respectively.

Expression and purification of SARS-CoV-2 spike proteins

We transfected plasmids (Addgene #154754) and expressed spike protein using Expi293 cells (Thermo Fisher A14527) using previously described methods (Hsieh et al., 2020). Briefly, we purified variants from 40 mL of cell culture. We filtered the supernatant using a 0.22-μm filter and ran it through a StrepTactin Superflow column (IBA 2-1206-025). We further purified spikes via Superose 6 Increase 10/300 (GE GE29-0915-96) size-exclusion column chromatography with a buffer containing 2 mM Tris at pH 8.0, 200 mM NaCl, and 0.02% NaN₃. We kept purified samples at 4°C and -20°C for short and long-term storage, respectively.

HEK293T transfection

We seeded cells into 6 or 12-well polystyrene-coated plates (VWR 10861-696, 10861-698) at a density of 0.3×10^6 cells mL⁻¹ or 0.1×10^6 cells mL⁻¹, respectively, one day before transfection. At 60–80% confluence, we used Lipofectamine 3000 (Invitrogen L3000015) and Opti-MEM (Gibco 51985091) to transfect cells with expression plasmids (3 μL of lipofectamine per μg of plasmid DNA) according to manufacturer instructions. At 48 h post-transfection, we assayed or collected the cells.

Flow cytometry and data analysis

At 48 h post-transfection, we collected HEK293T cells containing surface-displayed spike. We washed cells once with PBS and used gentle pipetting to resuspend them in PBS. We used the LUNA-II Automated Cell Counter (Logos Biosystems L40002) cell counter to determine cell density and spun cells down at 200 g for 1 min. We next decanted the supernatant and resuspended cells to a density of $\sim 3 \times 10^6$ cells mL⁻¹ in chilled PBS-BSA using 1% BSA (Sigma-Aldrich A3294), 1X PBS, and 2 mM EDTA at pH 7.4.

We used deep well grow blocks (Axygen P-2ML-SQ-C-S) to prepare flow cytometric assays. We added 1 μg mL⁻¹ Mouse anti-FLAG M2 (Sigma-Aldrich F3165) and predetermined concentrations of primary antibody or chimeric cell receptor (ACE2-Fc) diluted in PBS-BSA and 50 μL (1.5×10^5) of HEK293T cells to each well. We incubated the mixtures at room temperature for 1 h with shaking at 950 rpm. To pellet cells, we spun plates at 500 g in a swinging bucket rotor for 2 min. We then washed cells twice by decanting the supernatant and adding 500 μL of PBS-BSA to each well. To each well, we added 500 μL total volume of 5 μM Alexa Fluor 488 anti-mouse secondary (SouthernBiotech 1031-30) and 10 μM Alexa Fluor 647 anti-human secondary (SouthernBiotech 2048-31) antibodies in PBS-BSA. We incubated plates in the dark for 25 min at 4°C with shaking at 950 g. We washed each well twice with PBS-BSA and resuspended cells in PBS-BSA (300 μL) before loading them onto the SA3800 Spectral Cell Analyzer (SONY).

To establish forward scatter-area (FSC-A) and side scatter-area (SSC-A) gating, we used HEK293T cells. For singlet discrimination, we gated with forward scatter-height (FSC-H) vs forward scatter-area (FSC-A) and side scatter-height (SSC-H) vs side scatter-area (SSC-A). For each assayed sample, we acquired a minimum of 10,000 singlet events. We further analyzed singlet HEK293T cells using Alexa Fluor 488 (AF-488) and Alexa Fluor 647 (AF-647) channels with excitation and detection settings recommended by the manufacturer. To reduce spectral spill-over and autofluorescence effects, we applied spectral unmixing to all data.

For each sample, we measured the median height (*H*) for the AF-488 and AF-647 channels. To measure spike expression, we used the signal from the AF-488 channel (anti-FLAG). We used the following equation to calculate the expression of spike variant (*x*) relative to WT (6P-D614G):

$$\text{Normalized expression} = \text{Log}_2 \left(\frac{\text{Median : 488-}H_x}{\text{Median : 488-}H_{6P_D614G}} \right)$$

To correct for changes in transfection efficiency or spike expression in antibody or ACE2 binding measurements, we also included anti-FLAG signal as an internal normalization control. We used the following equation to calculate normalized binding measurements of spike variant (*x*) expression relative to WT (6P-D614G):

$$\text{Normalized binding} = \text{Log}_2 \left(\frac{\text{Median : 647-}H_x / \text{Median : 488-}H_x}{\text{Median : 647-}H_{6P_D614G} / \text{Median : 488-}H_{6P_D614G}} \right)$$

We used FlowJo v9 for all flow cytometry data analyses.

SARS-COV-2 authentic virus neutralization assay

To measure monoclonal antibody neutralization titers, we used a fluorescent focus reduction neutralization test (FFRNT) with an mNeonGreen (mNG) reporter SARS-CoV-2 (strain USA-WA1-2020) or SARS-CoV-2 (strain USA-WA1-2020) bearing a variant spike gene (Omicron BA.1). The construction of the mNG USA-WA1-2020 SARS-CoV-2 bearing variant spikes has been reported previously (Xie et al., 2021; Zou et al., 2022). For the FFRNT assay, we seeded 2.5×10^4 Vero E6 cells (ATCC CRL-1586) into black, μCLEAR flat-bottom 96-well plates (Greiner Bio-One 655096). We incubated plates at 37°C with 5% CO₂ overnight. The next day, each sample was two-fold serially diluted in culture medium with an initial dilution of 1:20. We incubated diluted antibody with 100–150 fluorescent focus units (FFU) of mNG SARS-CoV-2 at 37°C for 1 h before

loading the serum-virus mixtures into 96-well plates pre-seeded with Vero E6 cells. Following a 1 h infection period, we removed the inoculum and added overlay medium (100 μ L DMEM + 0.8% methylcellulose, 2% FBS, and 1% penicillin/streptomycin). We then incubated the plates at 37°C for 16 h and acquired raw images of mNG fluorescent foci using a Cytation™ 7 (BioTek) cell imaging reader with a 2.5 \times FL Zeiss objective and wide field of view. We used GFP software settings [469 nm, 525 nm], a threshold of 4000, and an object selection size of 50-1000 μ m during image processing. For relative infectivity calculations, we counted and normalized the foci in each well relative to non-antibody-treated controls. We plotted curves of relative infectivity versus serum dilution using Prism 9 (GraphPad). We used a nonlinear regression method to determine the dilution fold at which 50% of mNG SARS-CoV-2 was neutralized, defined as FFRNT₅₀ in GraphPad Prism 9. Each antibody was tested with two biological replicates.

Biolayer Interferometry

After 3C protease-mediated cleavage (Thermo Fisher 88946), we diluted supernatants containing spike variants two-fold with BLI Kinetics Buffer containing 10 mM HEPES at pH 7.5, 150 mM NaCl, 3 mM EDTA, 0.05% v/v Surfactant P20 (Cytiva BR100054), and 1 mg mL⁻¹ BSA. We also serially diluted analytes with the BLI buffer. We hydrated anti-mouse Fc capture (AMC) biosensors (FortéBio 18-5088) in BLI buffer for 10 min in an Octet RED96e (FortéBio) system and then immobilized mouse anti-FLAG M2 (Sigma-Aldrich F3165) antibodies to the AMC sensor tips. For each assay, we performed the following steps: 1) baseline: 60 s with BLI buffer; 2) IgG immobilization: 360 s with anti-FLAG IgG; 3) spike loading: 360 s with diluted supernatants; 4) baseline: 300 s with BLI buffer; 5) association: 600 s with serially diluted analytes (antibodies or ACE2); 6) dissociation: 600 s with BLI buffer. We used Octet Data Analysis software v11.1 with steady-state analysis to reference-subtract and analyze the data.

Differential Scanning Fluorimetry

Sample solutions containing 5X SYPRO Orange Protein Gel Stain (Supelco S5692) and 0.15-0.20 mg/mL of purified spike protein were added to a 96-well qPCR plate (Corning AXYPQR96LC480WNF). Fluorescence measurements were obtained continuously using λ_{ex} =465 nm and λ_{em} =580 nm, using a Roche LightCycler 480 II (Roche), and a temperature ramp rate of 4.5°C/minute increasing from 22 °C to 95 °C. Fluorescence data were then plotted as the derivative of the melting curve as a function of temperature (-dF/dT). SARS-CoV-2 spike proteins generate two local minimums that we report to as Tm1 and Tm2. All data were visualized in GraphPad Prism 9.

Computational analysis of GISAID sequence data

To investigate the clinical frequency of SARS-CoV-2 spike mutations and the probability of mutation co-occurrences, we performed pairwise amino acid sequence alignments between the GISAID spike reference sequence (GenBank number QHR63250.2) and all GISAID EpiCoV database SARS-CoV-2 spike amino acid sequences. We downloaded amino acid sequences from GISAID (accessed on December 18, 2021) as a FASTA file. We performed semi-global amino acid sequence alignment using MATLAB's Needleman-Wunsch alignment function as a part of its Bioinformatics Toolbox add-on. We set alignment parameters to include no gap open penalty at the beginning and end of sequences, an internal gap open penalty of 5, a gap extension penalty of 2, and the BLOSUM80 scoring matrix, as the aligned sequences were similar.

We filtered alignment pairs to remove all sequences that were non-human in origin, sequences containing over 1280 or fewer than 1260 amino acids, and sequences containing more than 800 unknown ("X") amino acids. We identified non-synonymous mutations from the alignments. The following equation was used to find frequencies for each mutation:

$$\text{Frequency} = \frac{\sum(\text{Sequences containing a specific mutation})}{\sum(\text{all mutations in all sequences})}$$

We found mutations that occurred independently by removing all alignment pairs that did not contain the target mutation and sequences that contained mutations other than the target mutation. Additionally, we considered alignment pairs for which the only other mutation (other than the target) was D614G were as independent, as D614G was highly prevalent in all strains after its initial appearance. The following equation was used to calculate frequency for independent mutations:

$$\text{Frequency} = \frac{\sum(\text{Sequences containing only the specified mutation})}{\sum(\text{all mutations in all sequences searched})}$$

Structural analyses and data visualization

We downloaded all structures (7DDN (Zhang et al., 2021), 7C2L (Chi et al., 2020), and 7JZL (Cao et al., 2020)) as PDB files from the RCSB PDB and imported them into ChimeraX 1.1. We rescaled the Log₂ (normalized binding) values (-7 to 0 or -1 to 0) and converted them to monochromatic ChimeraX color codes representing changes in binding relative to 6P-D614G spike. Dark red indicates decreased binding and white indicates no change in binding. For every amino acid screened in our Spike Display assay, we superimposed these colors scales onto spike protein structures. In figures showing grouped antibody epitopes, we averaged normalized binding values for all mutations in each position for every antibody comprising that group. Finally, we converted the averaged binding values to a single color that was then mapped onto spike structures.

QUANTIFICATION AND STATISTICAL ANALYSIS

The means \pm standard deviations (S.D.) were calculated and reported for all flow cytometry data, using two or more biological replicates. All DSF fluorescence data were plotted as the derivative of the melting curve as a function of temperature ($-dF/dT$). We used a nonlinear regression method to determine the IC₅₀ values for the BA.1 virus neutralization assays, defined as FFRNT₅₀ in GraphPad Prism 9. For every neutralization assay, antibodies were tested with two biological replicates.